AIAA Aviation
13-17 June 2016, Washington, D.C.
34rd AIAA Applied Aerodynamics Conference

2016-3725

Wake Deceleration of a Racecar Multielement Airfoil in Ground Effect

Suraj Bansal,* and Michael S. Selig†
University of Illinois at Urbana-Champaign, Urbana, IL 61801, USA

The importance of aerodynamic downforce in competitive motorsports has been well established. Much of this aerodynamic downforce is produced from the inverted multielement wings at the front and the rear of the car. While such a high-lift system is capable of producing high downforce as a result of the interaction between flows around adjacent elements, there may exist off-the-surface flow reversal, commonly known as wake bursting, causing an adverse effect on the downforce generated. Since the phenomenon of off-the-surface flow reversal occurs as a result of retardation of a wake under adverse pressure gradients, wake bursting is also referred to as wake deceleration in this study. A steady-state two-dimensional CFD analysis of a racecar multielement airfoil was carried out to study wake deceleration characteristics in ground effect. Simulations were performed using ANSYS® Fluent™, which is a finite-volume method (FVM) based commercial hybrid-grid Reynolds-averaged Navier-Stokes (RANS) equations solver. Computational results were obtained using a two equation shear stress transport (SST) k–ω model coupled with a one equation intermittency transition model to predict the laminar-to-turbulent boundary layer transition. The effects of ground clearance height on the main element decelerated wake were analyzed. The effects of varying flap ratio, flap deflection, angle of attack, and gap sizes on the wake deceleration patterns have been investigated. It was found that decreasing the ground clearance led to a significant increase in the amount of the main element wake bursting. Increased wake bursting at higher angles of attack was found to have caused a drop in downforce without any surface-flow separation. Although the main element wake was strongly affected while varying each of these parameters, the size of the flap wake was not affected significantly.

Nomenclature

c	=	system chord length
c_1	=	main element chord length
c_2	=	flap chord length
C_d	=	two-dimensional drag coefficient
C_l	=	two-dimensional downforce coefficient
h	=	ground clearance height
$l_{s,x}$	=	overhang distance
$l_{s,y}$	=	gap size
M_∞	=	freestream Mach number
N	=	total number of cells in the grid
p_∞	=	freestream static pressure
Re	=	Reynolds number based on system chord length
Re_θ	=	transition momentum thickness Reynolds number
T_∞	=	freestream static temperature
u	=	velocity component in x-direction
v	=	velocity component in y-direction
α	=	angle of attack
δ_f	=	flap deflection angle
γ	=	intermittency
ρ	=	density of air

*Graduate Student, Department of Aerospace Engineering, 104 S. Wright St., AIAA Student Member. sbansal5@illinois.edu
†Professor, Department of Aerospace Engineering, 104 S. Wright St., AIAA Associate Fellow. m-selig@illinois.edu

I. Introduction

Aerodynamic downforce is one of the most important factors when it comes to the design of a racing car. Since a large portion, typically 55–65%,[1] of the total aerodynamic downforce is produced by the inverted multielement wings installed on the racecar, the design of such high-lift devices becomes extremely important for maximum performance during the competition. Modern racecar design engineers strive to improve the multielement airfoil design in order to maximize the generated downforce, while satisfying all the geometric constraints imposed upon the wing geometry. The flowfield around multielement high-lift devices, largely influenced by viscous effects, is a complex one containing regions of high flow turning, merging flows, confluent boundary layers, flows through the slot, and wake bursting.[2,3] Introducing ground effect in such a complex flowfield will lead to an even more intricate flow dominated by these viscous effects. The study of multielement airfoils in ground effect thus becomes imperative.

The study of high-lift multielement airfoil flows in ground effect with respect to motorsports applications has attracted much attention in the literature. Razenbach et al.[4] experimentally and computationally studied a specific case of an inverted NACA 63_2–215 Mod B airfoil with a 30%c single-slotted flap to determine the differences produced in the flowfield with road conditions and wind tunnel ground boundary condition at a Reynolds number $Re = 1.5 \times 10^6$. On comparison of the experimental data with computational results, it was found that in both cases an increase in downforce was seen when decreasing ground clearance height, until a critical height was reached beyond which the downforce was reduced. The reduction in downforce was attributed to the merging of airfoil and ground boundary layers, thus altering the velocity and pressure fields in the region between the two surfaces. The authors[4] concluded that RANS computation with moving floor ground boundary condition is an extremely useful tool in analysis of such flows. Soso and Wilson[5] performed a downforce sensitivity analysis of the UIUC700 two-element airfoil using the commercial CFD software ANSYS® Fluent™. It was observed that with increasing main element angle of attack, downforce sensitivity decreased while decreasing the maximum downforce generated. An observation made by the authors[4] relevant to this study was that changing the main element angle of attack while maintaining the same flap deflection, gap, and overhang values had an effect of producing a thicker main element wake. Also, increasing the main element angle of attack changed the onset of flow separation on the main element surface which affected the amount of downforce generated.

In addition to surface flowfield, off-the-surface flow in the presence of an adverse pressure gradient has a significant impact on the performance of a multielement airfoil, thus affecting the C_l and C_d produced.[6–15] When the main element wake traverses a region of high adverse pressure gradient as a result of flow turning around the flap, it gathers a greater momentum-deficit, causing it to slow down and become thicker. Increased wake thickness causes the surrounding flow streamlines to flatten, thus affecting the surface pressure distribution. Pomeroy and Selig[16] investigated off-the-surface flowfield of a three-element airfoil system using a 7-hole probe in a low-speed low-turbulence open-return-type wind tunnel of the University of Illinois at Urbana-Champaign to experimentally capture wake bursting over multiple elements. Wake measurements were collected using a 7-hole probe to determine all three components of flow velocity along with pressure. It was found that an increase in the main element angle of attack led to a thicker-wake and an increased momentum deficit. Smaller gap sizes, larger overhang distances, and increased flap deflection angle amplified the amount of wake bursting.

Klausmeyer and Lin[8] analyzed the skin friction over a three-element supercritical airfoil with a leading-edge slat and trailing-edge flap using a two-dimensional RANS computational method at various angles of attacks and Reynolds numbers. The solver was finite-element method based and utilized unstructured triangular cell elements for computations. The Spallart-Allmaras turbulence model was employed to simulate the flowfield using a grid containing 55,000 nodes with a wall $y^+ = 0.5$. Results were obtained for a chord Reynolds number ranging from $5 - 6 \times 10^6$ over an angle of attack ranging from −4 to 24 deg. Loss of lift at higher angles of attack without surface-flow separation was observed. The loss of lift was attributed to the presence of a flow-reversal region in the main element burst wake. On increasing the angle of attack further, flow separation on the airfoil surface was observed as well. Similar observations by Johnston and Horton[17] and Nakayama et al.[6] have been reported.

Mahon and Zhang[18] computationally investigated 2-D flow around an isolated inverted two-element airfoil in ground effect. The main element airfoil was a derivative of NASA/Langley LS_1–0413 MOD profile with a finite trailing edge while the flap airfoil was typical of one usually used in motorsports. A multiblock hybrid grid, refined in areas of importance, was used to perform RANS simulations coupled with realizable k–ϵ model for modeling turbulence. The computational grid had 184,335 cells with wall $y^+ \approx 1$. A number of ground clearance heights were used to run the simulations in order to study variations in surface pressure distributions, aerodynamic forces, and off-the-surface flowfield. With respect to off-the-surface flowfield, the authors[18] reported that the wake thickness

increased with a decreasing ground clearance, and that the recirculation region aft of the main element finite-trailing edge greatly contributed to increased wake bursting. It was hypothesized that the use of a sharp main element trailing edge will cause a reduction in the wake thickness.

Despite a growing interest in understanding wake bursting, there still exists a gap in the existing literature regarding effects that the burst wakes have on the performance of an inverted multielement airfoil in ground effect with respect to application in the motorsports industry. A statement by Agathangelou and Gascoyne[1] shows the importance of analyzing the multielement airfoil wakes and tuning them for increasing the aerodynamic performance of a racecar:

> "Due to the fact that the rest of the car operates in the wake generated by this wing, and that this wake severely affects [sic] in particular the undertray and diffuser of the car, it is important to tune the wake profile of the front wing."[1]

The objective of this study was to build on a previous related work by Carroll[19] and to computationally capture wake deceleration patterns of the inverted two-element airfoil system in ground effect, and to determine different parameters that affect the development and behavior of these decelerated wakes. Effects of wake bursting on the performance of various two-element airfoil configurations with varying parameters were investigated by analyzing surface pressure distributions, sectional aerodynamic forces, velocity contours, and flow streamlines.

II. Geometry and Computational Grid

A. Airfoil Geometry and Definitions

An inverted two-element airfoil UIUC1600[19] that is typical of wings found on open wheel racecars was selected for this study, and the geometry is shown in Fig. 1 (see Appendix A for coordinates). The main element chord length c_1 is defined as the length of a line joining the leading and the trailing edge of the main element. The flap chord length c_2 is also defined in a similar fashion. In this study, the system chord length c is set to 13 in. and is defined as $c_1 + c_2$ when both the elements are set at zero angle of attack and placed end to end. To maintain this chord length at a fixed value of 13 in., the flap was increased in size whenever the main element size was reduced to vary the main element to system chord ratio, thereby defining a new airfoil in each case. The angle of attack α is defined as the angle made by the main element chord with the ground plane and is positive when its trailing edge is deflected upward with respect to its leading edge. The gap size $l_{s,x}$ was defined as the minimum distance of the flap from the main element trailing edge while the overhang distance $l_{s,y}$ was defined as the distance of the flap leading edge from the main element trailing edge along the main element chord, as shown in Fig. 1. A positive overhang is a case when the leading edge of the flap is upstream of the trailing edge of the main element, and a negative overhang is when the flap leading edge is aft of the main element trailing edge. The flap deflection angle δ_f is the angle made by the flap chord relative to the main element chord and is defined positive when the flap trailing edge is deflected upward. Finally, the ground clearance height h is defined as the shortest distance from the ground to the the main element airfoil. Table 1 shows the parameters defining the baseline configuration.

B. Computational Grid and Turbulence Model

Including the laminar-to-turbulent boundary layer transition modeling capability in CFD simulations has proven to be difficult in the past, and this has been particularly true in the case of general commercial CFD software used to simulate problems having real-life applications. As a result of this difficulty in modeling the boundary layer transition, many CFD simulations assume a fully turbulent boundary layer and hence fail to accurately capture the flowfield. Simulation of the laminar-to-turbulent boundary layer transition on high-lift devices is of great importance in acquiring accurate predictions.[14,20] Accurate modeling of the boundary layer transition process will lead to improved predictions of surface-flow separation which is critical for an accurate aerodynamic analysis of a high-lift system. In this study a 3-equation intermittency (γ) transition SST model[21] is used to simulate the UIUC1600 in ground effect. As discussed by Menter et al.,[21] the γ transition model has many advantages over the popularly used 4-equation γ–Re_θ transition model including reduced computational time while maintaining all the benefits of the Local Correlation-based Transition Model (LCTM) concept. Meshing guidelines for the γ transition model require wall y^+ to be nearly 1 for accurate resolution of wall boundary layers and prediction of transition, with at least 30 boundary layer cells in the normal direction and a growth rate of 1.1 or below required for grid independence.[21] A growth rate of 1.1 implies that the cell height of the $n + 1^{th}$ boundary layer will be 1.1 times the height of the n^{th} boundary layer cell.

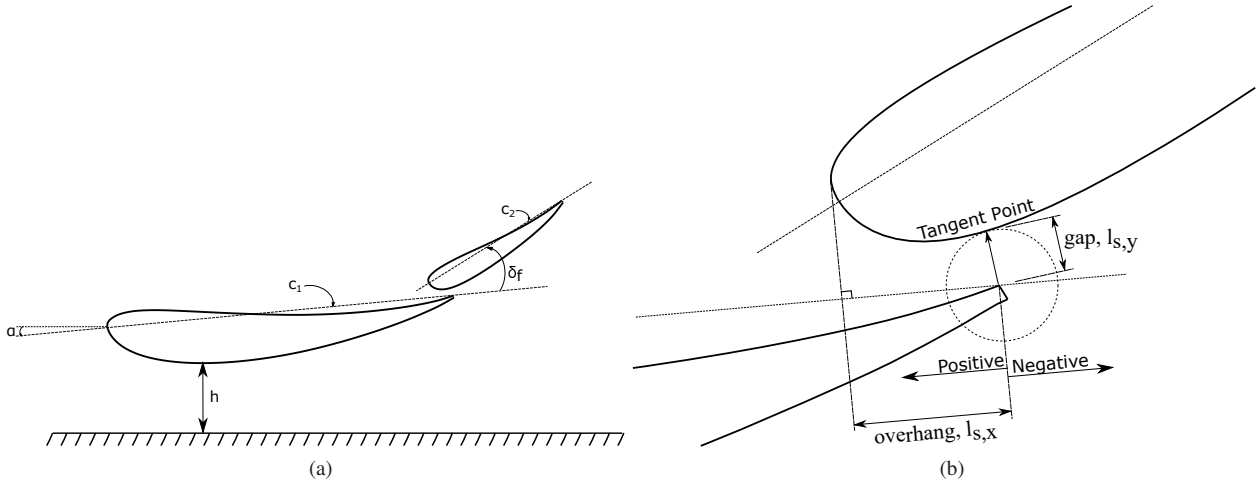

Figure 1. Diagram of the inverted multielement airfoil configuration UIUC1600 in ground effect showing (a) the full geometry and (b) a close-up of the gap size and overhang distance.

1. Grid Convergence Study

A systematic grid convergence study was conducted for an inverted two-element airfoil in ground effect, and the criteria used to determine the best grid to perform further simulations has been described. Four grids for the same geometry, 1) extra-coarse, 2) coarse, 3) fine, and 4) extra-fine grid, having progressively smaller cell sizes have been used to perform the grid convergence study (grids shown in Fig. 2). The total number of cells in the four grids are tabulated in Table 2. The grids were refined by prescribing smaller cell sizes on the airfoil and ground surfaces, by increasing the number of cell layers and using a smaller growth rate in the boundary layer mesh, and by decreasing the growth rate for the triangular cells in the inviscid region. The aforementioned parameters were carefully selected to maintain the smoothness of mesh by ensuring smooth transition from quadrilateral cells in the boundary layer to triangular cells in the inviscid region and by avoiding any abrupt change in the size and volume of the adjacent cells.

Grid convergence index (GCI) is a factor that aids in quantifying the computational uncertainty in a grid convergence study and provides a uniform method of presenting grid refinement results in the field of computational fluid dynamics. In this approach involving a grid convergence factor as proposed by Celik et al.[22] and Roache,[23] the true solution is extrapolated using the Richardson extrapolation method, and the computed solutions on successively refined meshes must approach the true solution asymptotically as shown in Fig. 3. The error bars shown in Fig. 3 are computed using GCI values determined using the approach described in Celik et al.[22]. These error bars represent the

Table 1. Tabulated Values of Various Baseline Configuration Geometric Parameters for the UIUC1600

Parameter	Value
System chord, c	13 in.
Ground clearance height h	4 in.
Angle of attack α	5 deg
Flap deflection angle δ_f	27 deg
Main element to system chord ratio (c_1/c)	69%
Flap element to system chord ratio (c_2/c)	31%
Gap size $l_{s,x}$	0.211 in.
Overhang distance $l_{s,y}$	0.595 in.

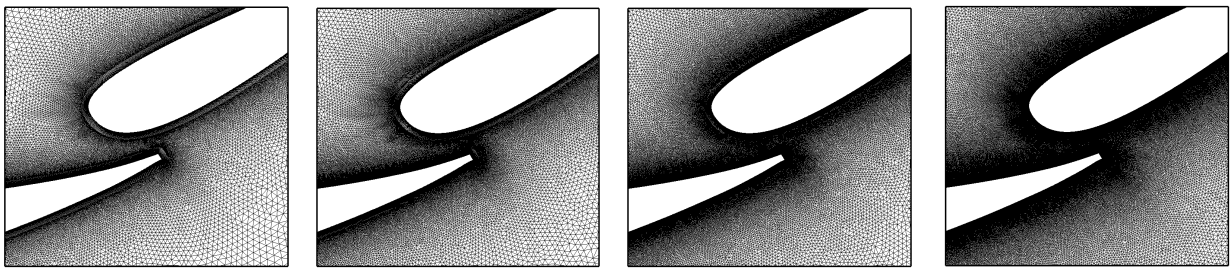

Figure 2. Computational grids for the two-element airfoil UIUC1600: (a) extra-coarse grid, (b) coarse grid, (c) fine grid, and (d) extra-fine grid.

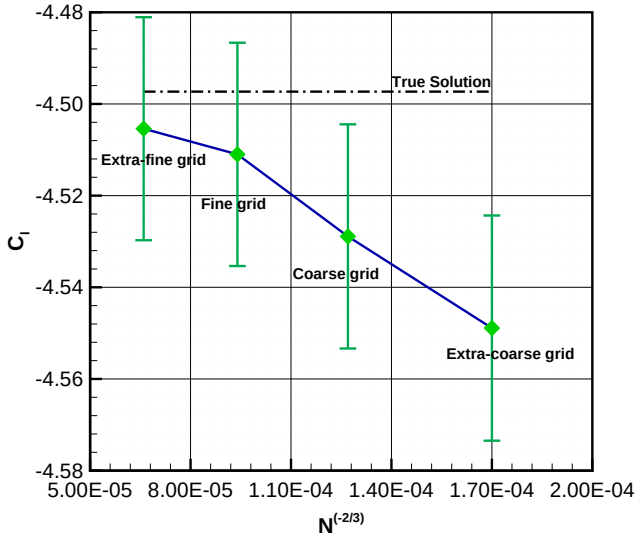

Figure 3. Grid convergence of C_l from the SST γ transition model.

amount of uncertainty in the computed solution. If the true solution falls within the uncertainty range of the computed solution from a given mesh, the mesh is suitable for use in further simulations.

2. Grid Selection

The data from Fig. 3 indicate that the fine and extra-fine meshes are suitable for further computations. Given the availability of limited computational resources, the fine grid was selected as the converged grid for the remainder of this study. Figures 4–5 show the fine grid in greater detail.

The inlet, outlet, and the far-field boundary of the computational domain are both maintained at a distance of $32c$ from the airfoil surfaces to ensure a good mesh quality and to allow full development of the wake. The ground clearance height was set according to the case being simulated. A hybrid computational grid, as shown in Fig. 4, was generated using a patch conforming advancing front approach with (1) structured cells containing quadrilateral elements near the airfoils and ground to capture the boundary layer on each surface and (2) unstructured triangular cells filled in the remaining space of the computational domain.

The centroid of the first boundary layer cell on the main element, flap, and ground was set to achieve a maximum wall y^+ value less than 1, as required by the γ transition SST model for accurate resolution of the boundary layer. The boundary layer cell growth rate was set at 1.04 for the airfoil and 1.07 for the ground boundary layer mesh. The boundary layer meshes had 85 layers of cells normal to both the main element and flap surfaces and 65 layers of

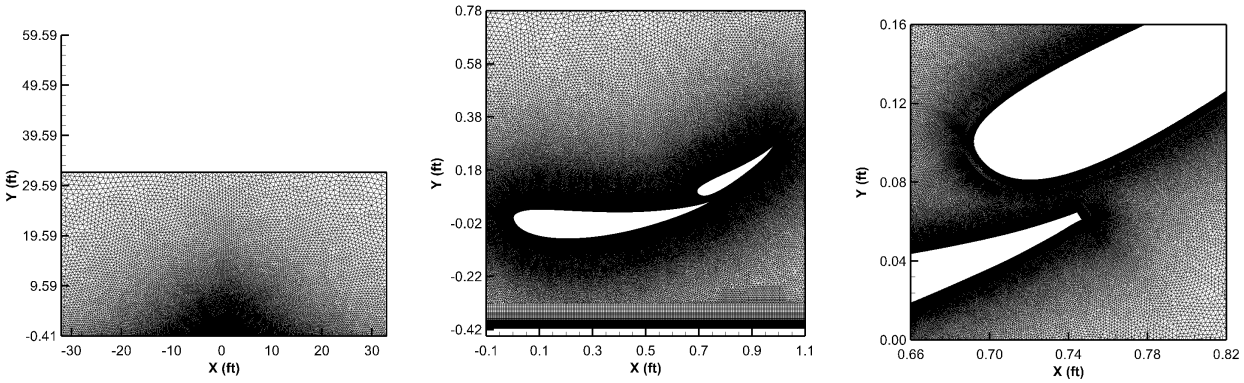

Figure 4. Computational grid for the two-element airfoil UIUC1600: (a) computational domain, (b) grid refined in relevant regions around the airfoil, and (c) fine grid cells between the gap.

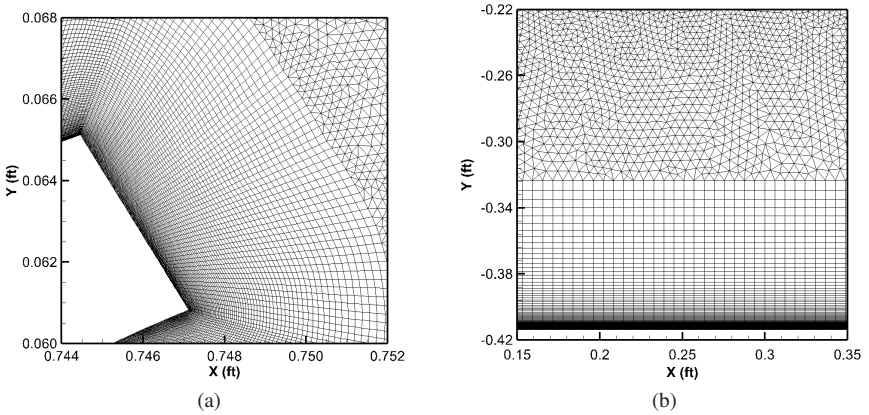

Figure 5. Boundary layer cells and transition to triangular cells: (a) airfoil surface and (b) ground surface.

cells normal to the ground. In order to capture the decelerated wakes accurately, the growth rate of the unstructured triangular cells was set at 1.035 to keep the cell size small in the vicinity of the multielement airfoil.

III. Results and Discussion

The wake deceleration characteristics of the UIUC1600 inverted two-element airfoil operating in ground effect have been simulated. The effects of individual parameters have been isolated by varying the ground clearance height, angle of attack, flap deflection angle, main element to system chord ratio, and gap size, while maintaining other parameters constant. Varying each parameter led to a different geometric configuration which was meshed separately each time. ANSYS® Fluent™ was used to perform the simulations on a desktop PC with an Intel® Core i7 quad core

Table 2. Tabulated List of the Total Number of Cells for Four Different Grids

Grid	Total number of cells, N
Extra-coarse grid	451,926
Coarse grid	698,652
Fine grid	1,103,664
Extra-fine grid	1,869,186

processor and 12 GB of RAM. The simulations were assumed to be converged when (1) the relative residual for each equation was below 10^{-6} and (2) there were no changes in C_l and C_d values for more than 1,000 iterations.

All cases were run at a fixed Reynolds number $Re = 1.1 \times 10^6$ based on the system chord length c, freestream Mach number $M_\infty = 0.15$, operating pressure $p_\infty = 2017.42$ lb/ft^2, and operating temperature $T_\infty = 518.69$ ^{o}R. The upstream boundary was modeled using velocity inlet boundary condition, with inlet velocity of 167.44 ft/s, inlet turbulence intensity of 0.07%, and inlet viscosity ratio of 10. The downstream boundary of the domain was modeled using pressure-outlet boundary condition in which the gauge pressure was set at zero. The domain farfield was modeled using pressure far-field boundary condition which enforced a velocity tangency condition. The ground was modeled using a moving-floor boundary condition or the road condition[4] in which the ground moves with the freestream velocity in the positive x-direction. Since the study deals with an inverted racecar multielement airfoil system, C_l will represent the aerodynamic downforce coefficient instead of the aerodynamic lift, with a negative sign denoting the downward direction of forces that are generated orthogonal to the freestream direction. Wake bursting occurs as a result of high velocity deficit gathered by the wakes under adverse pressure gradients, and hence the term wake deceleration has been interchangeably used with wake bursting in this study.

A. Effect of Ground Proximity

Racecar wings operate in strong ground effect producing a high aerodynamic downforce to improve traction. Additionally, the front wing is also used as a trimming device, and its sensitivity to the ground proximity determines the ease of driving a racecar. Studying the effect of ground proximity on the manner in which wakes of a high-lift airfoil system behave, thus becomes important. Hence, the flow around the UIUC1600 was simulated at varying ground clearance heights while maintaining the same values of other baseline configuration geometric parameters as defined in Table 1.

Figure 6 shows velocity contours for different ground clearance heights where the warmer shades (red) of color show higher velocity while cooler shades (blue) represent low velocity. As can be seen in Fig. 6b, the peak velocity on the suction surface of the main element increases when placing the airfoil in ground vicinity ($h = 12$ in.) compared with when the airfoil is out of ground effect. The peak velocity increases further with reduction in the ground clearance height until a height of 4 in. is reached, as represented by increasing intensity of the red color beneath the suction surface in Figs. 6b–6d. A ground clearance height of 4 in. is typical of front wings on an open-wheel racecar. The data indicate that further decreasing the clearance height leads to a reduction in the peak velocity on the main element airfoil as a result of flow separation on its suction surface. The blue regions beneath the flap represent main element wake deceleration due to the adverse pressure gradient as a result of the flow turning around the flap. With progressive reduction in ground clearance heights, the blue region grows larger indicating increased main element wake deceleration causing it to thicken. The separated flow from the main element surface merges with the decelerated main element wake when the airfoil is operating at $h = 1$ in. as shown in Fig. 6e. Although a racecar front wing will seldom operate at such low h values, small ground clearance heights may be experienced when the racecar pitches down, for example, when applying brakes. Upon close inspection of Fig. 6e, it becomes clear that any further decrement in the ground clearance may result in confluence of the burst wakes from the airfoil and the ground boundary layer. Thus, at extremely low ground clearance heights achieved when the car pitches down on the racetrack, the resulting confluence may affect the flowfield around the downstream aerodynamic components of the racecar and may cause handling problems.

The adverse effects of wake bursting on the aerodynamic performance of a multielement airfoil system becomes apparent from the data in Fig. 7. In this figure the streamlines are plotted uniformly around the multielement airfoil simulated at different ground heights in order to better visualize the flowfield. On careful inspection, one can notice the increased crowding of streamlines at the suction surface and a decrease in the same on the high-pressure surface of the main element indicating higher lift, as seen in Fig. 7b. Near the suction surface of the flap, the streamlines diverge due to wake thickening, causing the streamlines curvature to decrease. It is this decambering in the streamlines curvature near the flap, as a result of wake deceleration and subsequent wake thickening, that causes flap loads to become suppressed. The loss of streamline curvature is further increased as the ground clearance is decreased, as seen in Figs. 7b–7e, causing a greater reduction in the value of C_l. The downforce reduction is worsened when the wake of the main element merges with the separated region around its trailing edge, causing the load on a portion of the main element to be suppressed as well.

The flow structure of the main element wakes can be observed from Fig. 8 which presents zoomed-in plots of the streamlines in the vicinity of the flap. The wake deceleration is increased when bringing the airfoil closer to ground

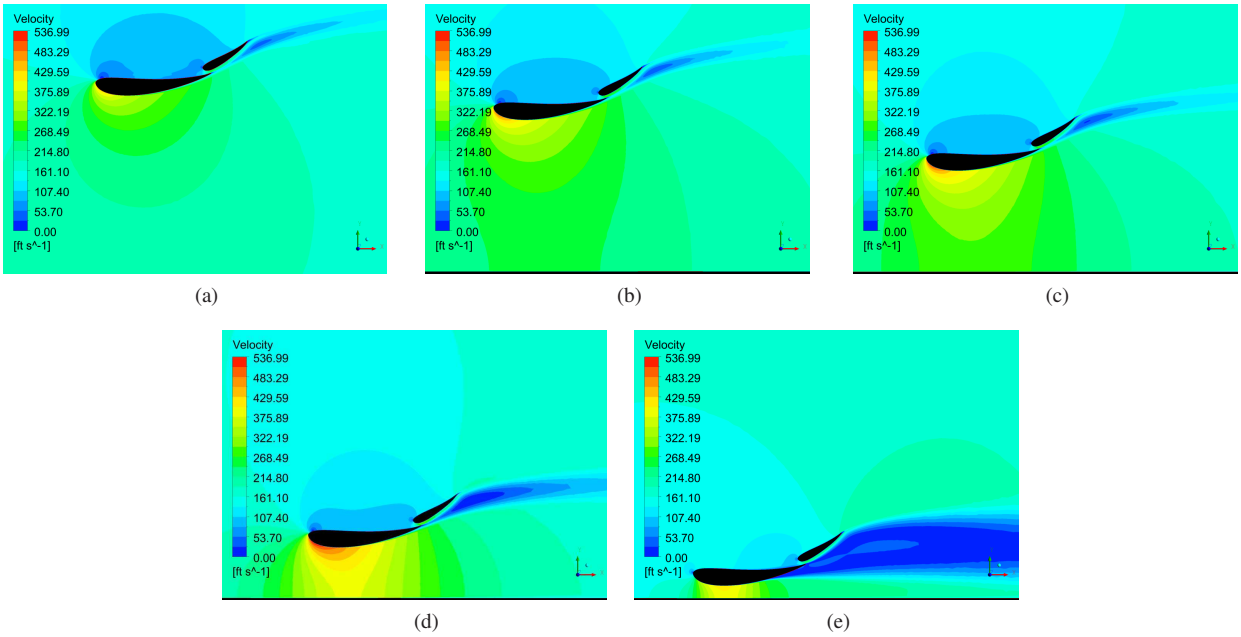

Figure 6. Plots of velocity contours depicting effect of ground proximity on wake bursting for five different ground heights: (a) no ground, (b) $h = 12$ in., (c) $h = 8$ in., (d) $h = 4$ in., and (e) $h = 1$ in.

causing the streamlines to diverge, as seen while comparing Figs. 8a–8d. When the ground clearance is reduced to 1 in., flow reversal is observed in the decelerated wake where the flow separates from itself to form two vortices. The lower vortex in the main element wake merges with the separated flow on the aft portion of the main element causing it to become larger in size than upper vortex. Also, the path-angle followed by the burst wakes is shallower causing the streamlines below the wake to flatten out further and the downforce to decrease.

The trends discussed above can be observed in the pressure distribution plots for varying ground clearance heights in Fig. 9. With smaller values of the ground clearance height, the suction peak on the C_p distribution plots increases until a height of 4 in. is achieved. The increase in the suction peak with reducing values of h is due to a venturi-like channel with converging and diverging cross-section areas formed between the airfoil and the ground, as seen in Figs. 6 and 7. The flow is accelerated in the converging area of the channel, thereby increasing the peak velocity on the main element and consequently the suction peak. Bringing the airfoil any closer to the ground results in the loss of suction peak due to flow separation. The flow separation is caused due to the high adverse pressure gradients in the diverging portion of the channel, and this causes the pressure distribution on the aft portion of the suction surface to become flat as observed in Fig. 9e. The location of the laminar-to-turbulent boundary layer transition on the main element and flap suction surfaces moves toward the leading edge with reduced ground clearance height and is due to the increased adverse pressure gradients at lower ground heights. The effects of wake bursting become evident when observing the C_p distribution around the flaps in Figs. 9d–9e. When the burst wakes are thick enough to cause significant decambering of the streamlines in the flap vicinity, the pressure on the flap suction surface increases causing the pressure distribution on the flap to plateau. The flattening of the flap C_p distribution contributes to the loss of overall downforce produced from the airfoil system. It is worth noting that the C_p distribution plots show the presence of a laminar separation bubble.

Figure 10 shows the lift and drag coefficient trends for varying ground clearance height h. As h is decreased to 12 in., an increase of 26.4% is observed in the aerodynamic downforce coefficient C_l value over the case with no ground present. The trend of increasing C_l with decreasing h continued until a clearance height of 4 in. was reached. The data indicate that decreasing the ground clearance below this point leads to a drastic decrement in the C_l value produced as shown in Fig. 10a. The drag coefficient C_d on the other hand shows a monotonically increasing pattern with decreasing ground clearance, as shown in Fig. 10b. The drag coefficient becomes significantly larger at $h = 1$ in. due to merging of an already thick decelerated wake with the separated flow from the main element.

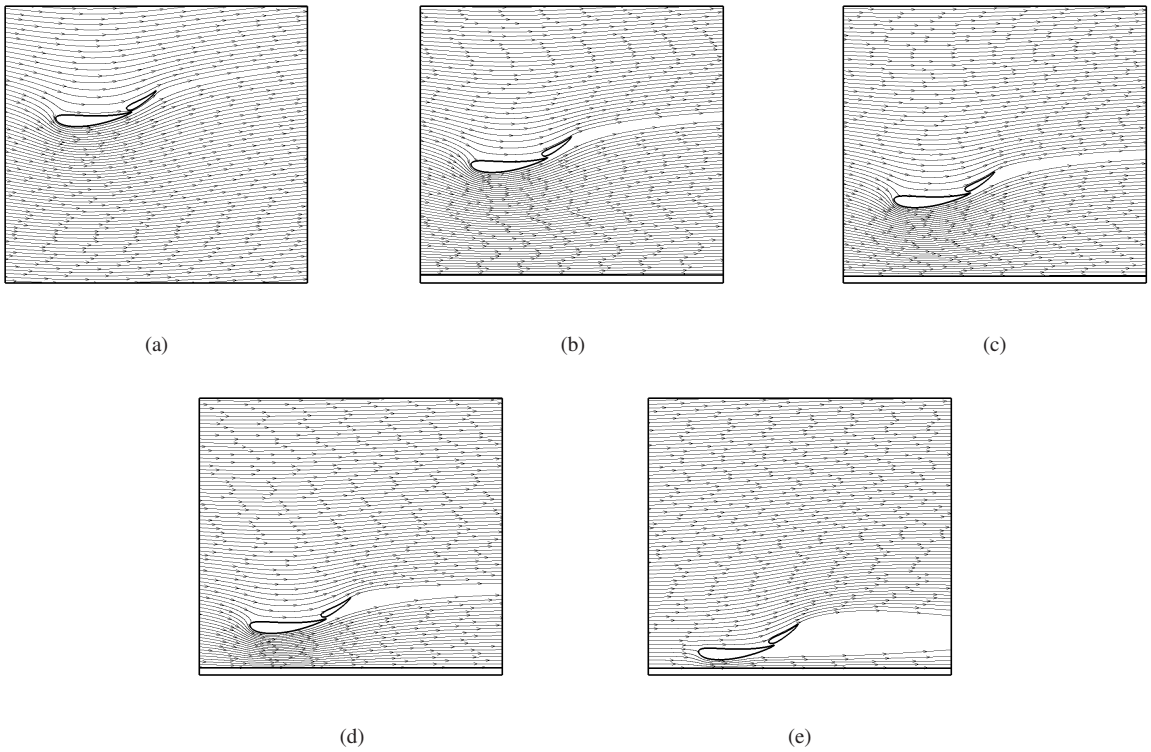

Figure 7. Streamlines around UIUC1600 at five different ground clearance heights: (a) no ground, (b) $h = 12$ **in., (c)** $h = 8$ **in., (d)** $h = 4$ **in., and (e)** $h = 1$ **in.**

B. Effect of Angle of Attack

The main element angle of attack was varied from −1 to 8 deg with the remainder of the baseline configuration parameters maintained at the same values as given in Table 1. Figure 11 shows the velocity contour plots for the UIUC1600 airfoil for these varying angles of attack. As can be seen from the data, with increasing angle of attack the intensity of the red region beneath the main element increases, indicating an increase in the peak velocity. This trend of increasing peak velocity with increasing α is observed until $\alpha = 5$ deg is reached, beyond which the peak velocity is reduced due to highly-separated flow. The velocity deficit gathered by the main element wake, as represented by the blue region beneath the flap, increases with increasing α and becomes significantly large at $\alpha = 8$ deg.

Figure 12 shows the flow streamlines around the multielement airfoil for different angles of attack. A fixed number of streamlines are plotted uniformly to represent the manner in which the flowfield behaves around the airfoil system. It is evident that the thickness of the main element wake increases with increasing angle of attack, as represented by the diverging streamlines beneath the flap in the figure. Figure 13 shows the main element wake structure for different values of α. The streamlines in the wake increasingly diverge with increasing α, indicating increased wake bursting due to higher adverse pressure gradient. When the angle of attack reaches a value of $\alpha = 8$ deg, flow reversal is observed in the main element wake causing two large vortices to form. Also, at $\alpha = 8$ deg, the flow separates from the main element suction surface near the trailing edge and merges with the burst wakes thus contributing toward an increase in the main element wake thickness.

Figure 14 shows results of all the cases simulated for varying angles of attack. It was observed that C_l increases with an increasing angle of attack before reaching a critical angle, beyond which a loss of downforce occurs. The critical angle of attack in this case was 2 deg with $C_{l,max} \approx -4.6$.

Figure 15 shows the pressure distribution plots for different angles of attack. The data indicate that as the angle of attack increases, the strength of the adverse pressure gradient increases both on the main element and the flap, causing the transition points on the suction surfaces to move upstream. The boundary layer flow on the main element is able to transition via a laminar separation bubble for all values of α, while a laminar separation bubble is formed on the flap

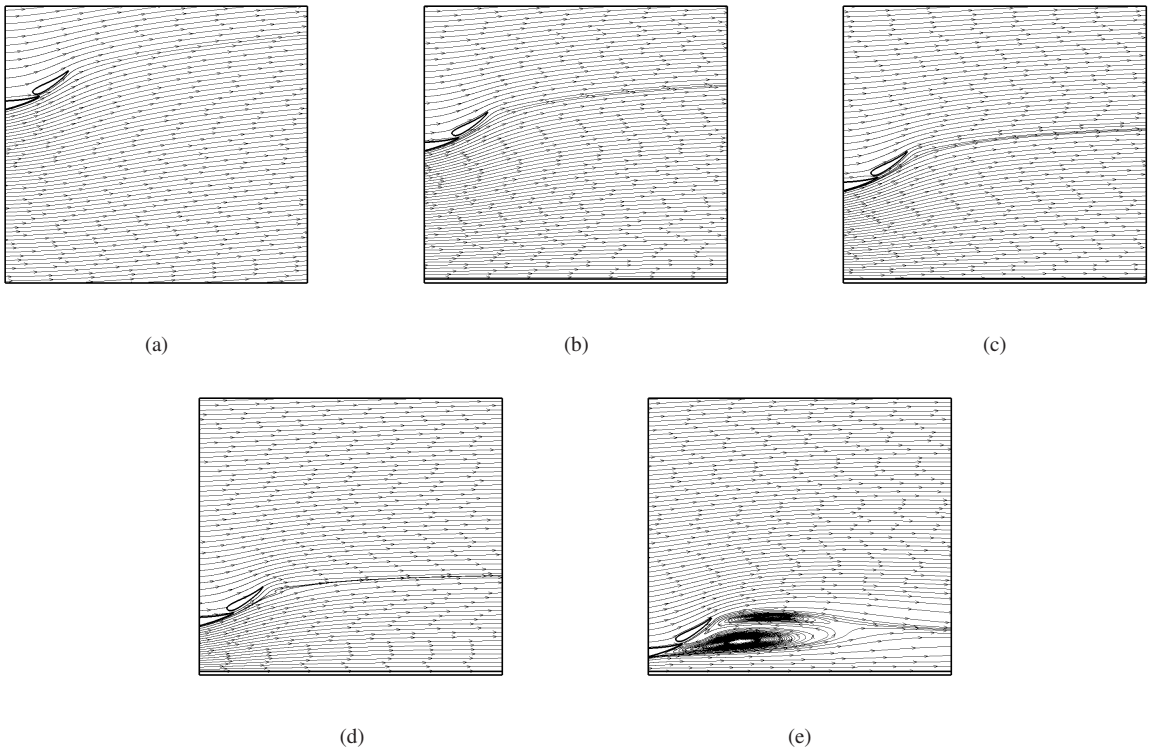

Figure 8. Effect of ground proximity on the degree of wake bursting, as shown by streamlines in the flap vicinity: (a) no ground, (b) h = 12 in., (c) $h = 8$ in., (d) $h = 4$ in., and (e) $h = 1$ in.

surface for $-1 \leq \alpha \leq 5$ deg. No transition on the flap is observed on the flap surface for $\alpha = 8$ deg.

An interesting observation can be made upon careful examination of the pressure distribution shown in Fig. 15. The loss of downforce occurs at $\alpha = 5$ deg with no flow separation observed on the main element or on the flap surface. In fact, $\alpha = 5$ deg has a higher suction peak on the main element than when the angle of attack has a value of $\alpha = 2$ deg. The main factor that drives C_l to a lower value at $\alpha = 5$ deg is the pressure distribution around the flap. On comparing Figs. 15c and 15d closely, a flatter flap pressure distribution can be observed for the latter case.

An explanation for the loss of downforce without flow separation on the airfoil surfaces can be explained with Fig. 12. On examining the flowfield, the manner in which the streamlines diverge below the flap suction surface with increasing α can be observed. As the main element wake loses velocity while traversing the adverse pressure gradient region around the flap, the streamlines become less crowded and diverge causing the neighboring streamlines to have less curvature. On recalling that the downforce is produced as a result of lower-than-freestream pressure on the airfoil suction surface due to the streamline curvature introduced by the airfoil geometry, it can be concluded that the loss in the streamline curvature around the burst wake results in increased pressure on the suction surface of the flap, thus causing the C_l value to fall. In substantial wake bursting, the curvature loss experienced by the surrounding streamlines will be greater thus increasing the pressure on the flap suction surface. The resulting increased pressure on the flap may be enough to reduce the overall downforce from the airfoil system despite the increase in the suction peak on the main element, thus demonstrating the significance of wake bursting on the aerodynamic performance of an inverted multielement airfoil in ground effect.

C. Effect of Main Element to System Chord Ratio

The size of the main element expressed as a percentage of the total chord is varied to study its effect on wake bursting and the downforce. As the main element was reduced in size, the flap size was increased to maintain the same value of the total chord, as defined earlier (13 in.). The range of the main element size varies from as large as 79% of the system chord c to as small as 49%, while keeping the other baseline configuration parameters constant.

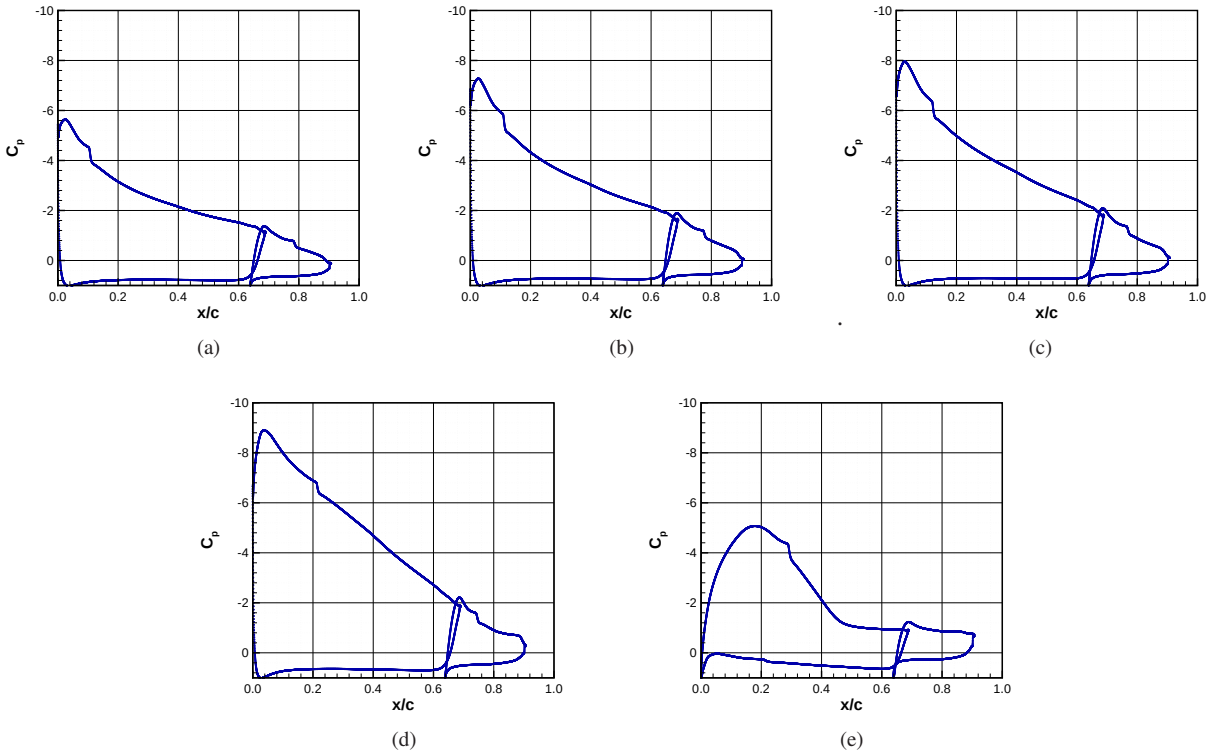

Figure 9. Pressure distribution plots for the selected multielement airfoil configuration at different ground clearance height: (a) no ground, (b) $h = 12$ **in., (c)** $h = 8$ **in., (d)** $h = 4$ **in., and (e)** $h = 1$ **in.**

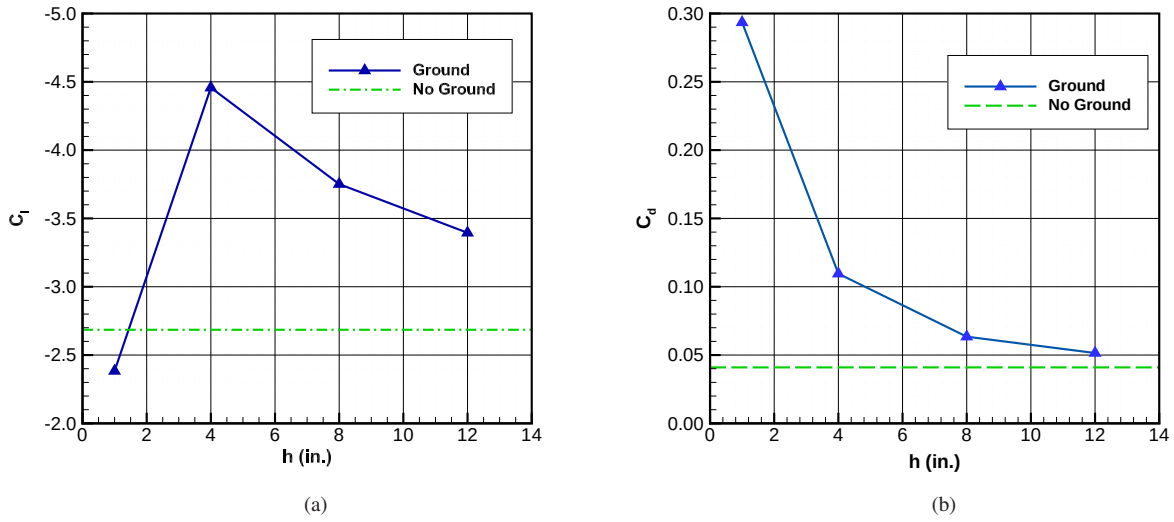

Figure 10. Variation of lift and drag coefficients with varying ground proximity.

Figure 16 shows the velocity contour plots for varying main element and flap sizes of the UIUC1600. As the flap size grows larger, the peak velocity on the main element suction surface increases as seen from the growing intensity of the red region beneath the main element. The blue region beneath the flap surface representing the main element wake deceleration grows larger in size and intensity with increasing flap size. Figure 17 shows the streamline plot for the

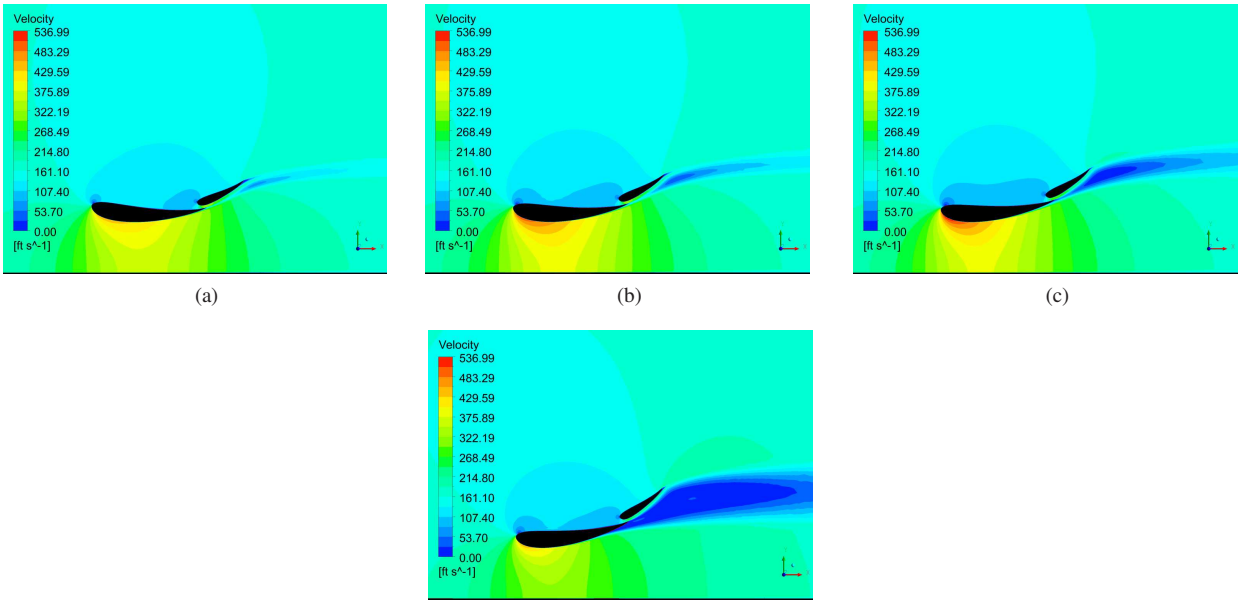

(a) (b) (c)

(d)

Figure 11. Velocity contours depicting effect of main element angle of attack on wake bursting: (a) $\alpha = -1$ **deg, (b)** $\alpha = 2$ **deg, (c)** $\alpha = 5$ **deg, and (d)** $\alpha = 8$ **deg.**

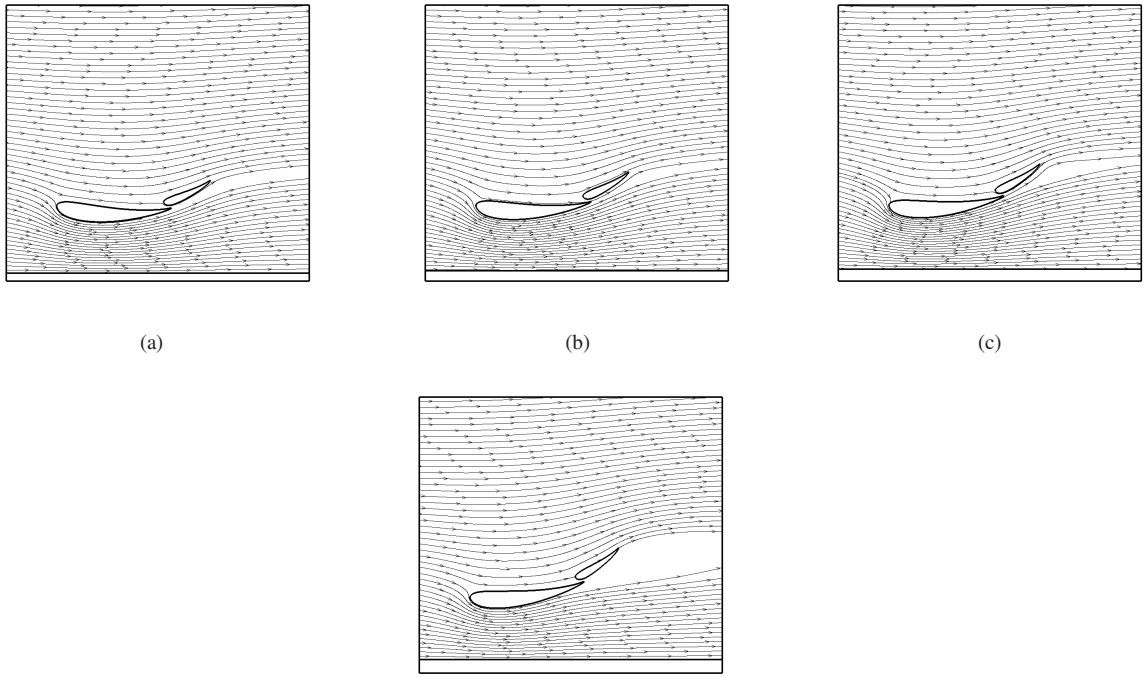

(a) (b) (c)

(d)

Figure 12. Diverging streamlines near the lower surface of the flap due to wake deceleration for four different main element angles of attack: (a) $\alpha = -1$ **deg, (b)** $\alpha = 2$ **deg, (c)** $\alpha = 5$ **deg, and (d)** $\alpha = 8$ **deg.**

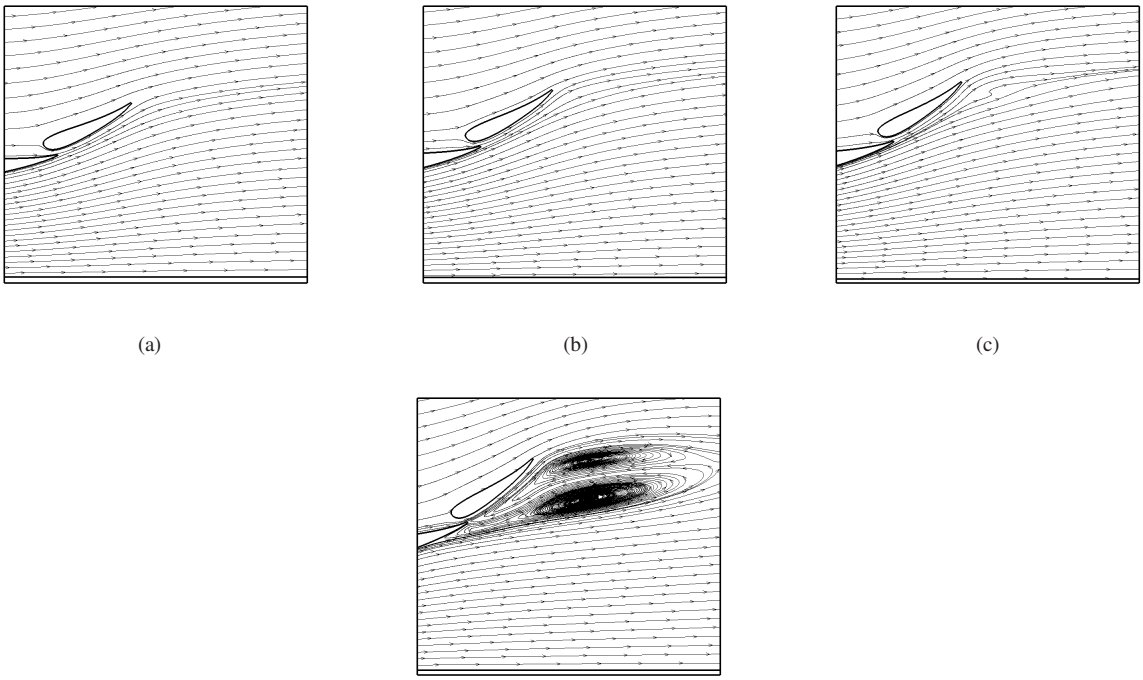

(a) (b) (c)

(d)

Figure 13. Effect of angle of attack on the degree of wake bursting, as shown by streamlines in the flap vicinity shown for four different angles of attack: (a) $\alpha = -1$ deg, (b) $\alpha = 2$ deg, (c) $\alpha = 5$ deg, and (d) $\alpha = 8$ deg.

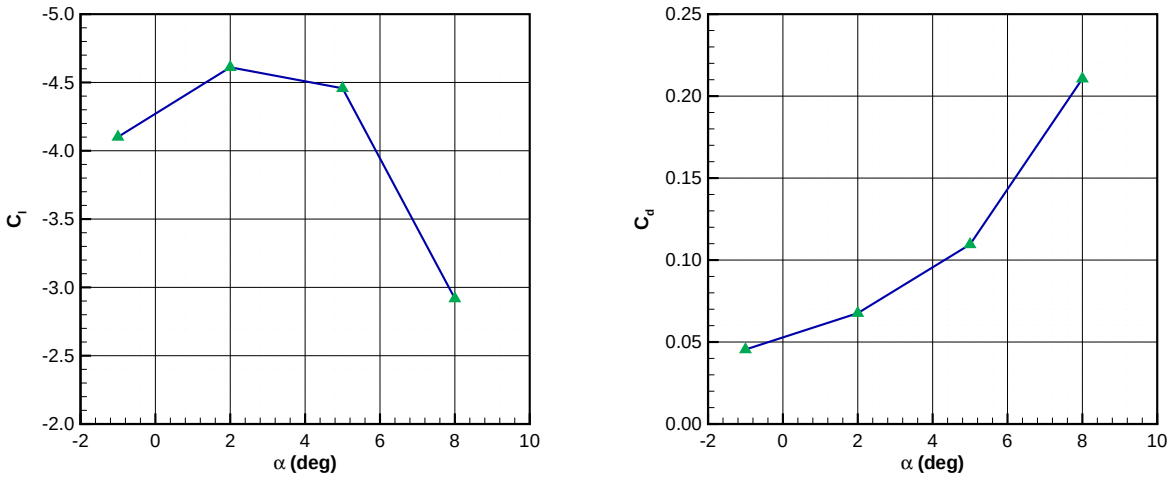

(a) (b)

Figure 14. Variation of lift and drag coefficients for the UIUC1600 airfoil with angle of attack.

UIUC1600 having different main element to system chord ratios. The streamlines are more crowded beneath the main element suction surface when the flap size is larger. Also, with increasing flap size the streamlines in the flap vicinity diverge by a greater amount indicating the presence of a thicker wake. Figure 18 shows the flow structure within the main element wake in greater detail. When the main element to system chord ratio is 79%, two small vortices are

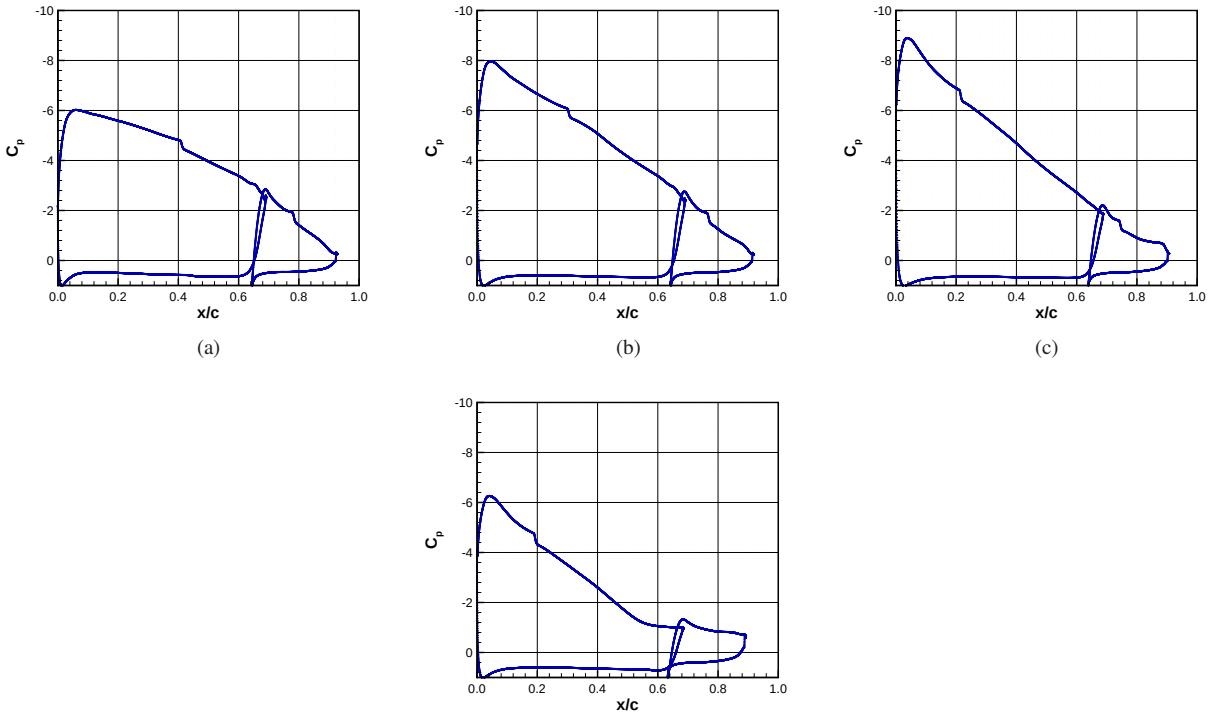

Figure 15. Variation of C_p distribution with angle of attack α: (a) $\alpha = -1$ deg, (b) $\alpha = 2$ deg, (c) $\alpha = 5$ deg, and (d) $\alpha = 8$ deg.

formed as a result of the off-the-surface flow separation in the main element wake. When the flap size is increased resulting in a main element to system chord ratio of 69%, the flow reversal in the wake is suppressed. The flow reversal is observed again for the main element to system chord ratios of 59% and 49%. When the flap is small in size (79% main element), the peak velocity on the main element suction surface is low and hence the resulting main element wake has low momentum to begin with, while traversing the adverse pressure gradient in the flap vicinity. It is this low momentum in the main element wake that results in flow reversal and the subsequent formation of two vortices. When the flap size is increased (69% main element), the peak velocity increases and hence the wakes from the main element have higher momentum before traversing the adverse pressure gradient beneath the flap which results in suppression of flow reversal. On increasing the flap size further (59% and 49% main element), the peak velocity on the suction surface increases but the resulting adverse pressure gradient in the flap region is high enough to cause off-the-surface flow separation within the wakes resulting in formation of the two vortices again. It should be noted from Fig. 16 that even though the smallest and the largest flap sizes result in flow reversal in the main element wakes, the intensity and the size of the blue region increases with increasing flap size indicating greater wake bursting.

The lift and drag results for the analysis are presented in Fig. 19. As the size of the main element decreases, an increase in the downforce coefficient C_l is seen until a main element to system chord ratio of 59%, beyond which C_l experiences a slight drop in value. The drag coefficient C_d on the other hand rises monotonically with decreasing main element size and is as a result of the larger exposed frontal area due to increased flap size.

Figure 20 shows the pressure distribution trends with a varying main element to system chord ratio. As the main element size is decreased, higher main element and flap suction peaks are observed. On careful examination of Fig. 17, the angle made by the line joining the leading edge of the main element and the trailing edge of the flap with the ground increases with a decreasing main element size. The aforementioned angle reflects the amount of curvature observed in the flowfield. Hence, with an increasing angle made by the line joining the leading edge of the main element and the trailing edge of the flap with the ground the streamlines around the flap experience a greater turning which increases the peak velocity on the flap and hence increases its circulation. An increase in the circulation on the flap in turn increases the main element suction peak due to the circulation effect, as described by Smith.[2] Also, with a decreasing

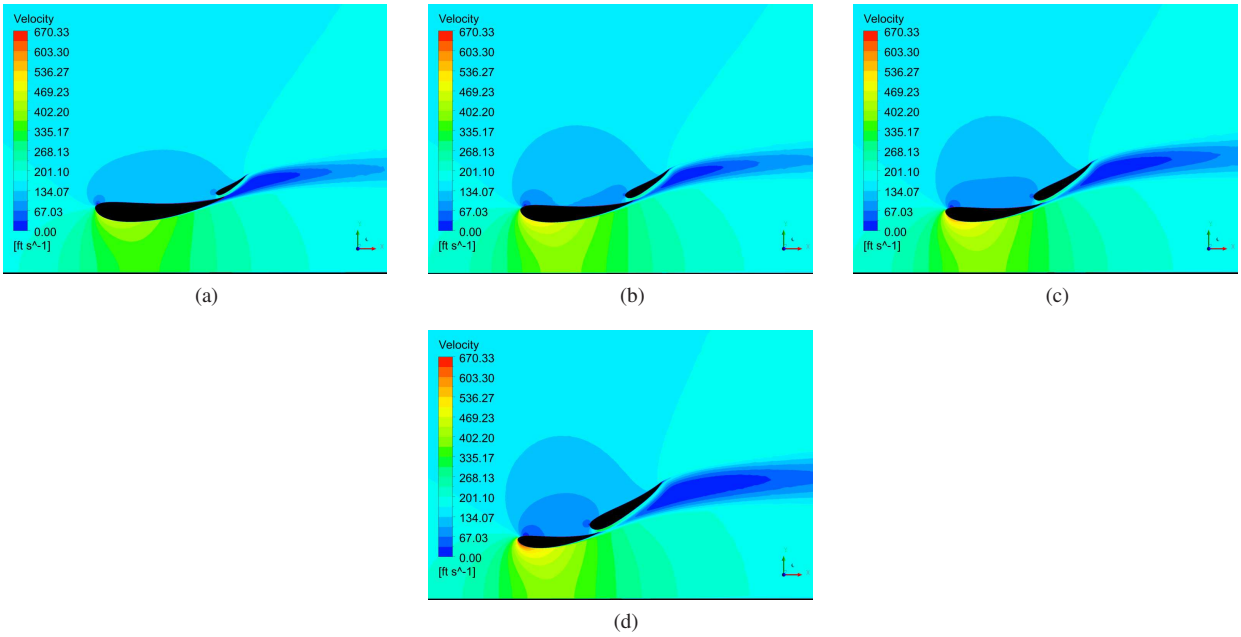

Figure 16. Velocity contours depicting wake bursting with varying main element to system chord ratio: (a) 79% main element, (b) 69% main element, (c) 59% main element, and (d) 49% main element.

main element size, the C_p curve in the recovery region on the flap suction side becomes flatter as a result of an increase in the thickness of the burst main element wakes, shown in Figs. 16 and 17. The increasing flatness of the flap C_p distribution in the recovery region can be explained by looking at Fig. 16. As the main element size reduces, the flap size increases and so does the amount of wake bursting. As the flap grows larger, the low-momentum wake of the main element has to travel in the high-adverse pressure gradient region for a longer distance causing it to gather higher velocity deficit and become thicker. As explained earlier, this increased wake thickness affects the pressure distribution on the flap suction surface.

A competition between the positive interaction of the main element with the flap via circulation effect and the negative one via wake bursting is what causes the rate at which C_l increases to reduce with each decrement in the main element size. The significance of wake bursting in the performance of a high-lift system can be seen from Fig. 19. For the 49% main element case, the positive effect of an increase in the suction peak due to a larger flap was countered by larger amount of wake bursting, thus causing the C_l to be lower than the one in the 59% main element case, while drastically increasing the C_d.

D. Effect of Flap Deflection

The flap deflection angle effects on the wake bursting were analyzed for the UIUC1600 airfoil system for three deflection angles of 12, 27, and 42 deg while maintaining other baseline configuration parameter values as shown in Table 1. Figures 21 and 22 show that with increasing flap deflection the wake bursting increases, as indicated by the larger size and intensity of the blue region beneath the flap and the amount by which streamlines diverge indicating the increased wake thickness and decambering of flow streamlines in the flap vicinity. The peak velocity increases with increasing flap deflection angle until $\delta_f = 27$ deg, beyond which the peak velocity is reduced due to highly separated flow. Figure 23 shows the main element wake structure for varying flap deflection angles. With increasing values of δ_f, the flow streamlines in the wake diverge by a greater amount causing loss of curvature in the surrounding streamlines. At $\delta_f = 42$ deg, the flow separates from the main element suction surface and merges with the lower vortex formed in the main element wake, thus causing the decelerated wake to become larger in size.

Figure 24 summarizes the results of the simulations. The downforce coefficient C_l increases when the flap deflection is increased from 12 to 27 deg and decreases when δ_f is increased to 42 deg. The drag coefficient C_d increases monotonically with increasing δ_f as a result of a larger frontal area exposed to the incoming flow.

Figure 25 shows the pressure distribution plots for varying flap deflection angles. In general, increasing the flap

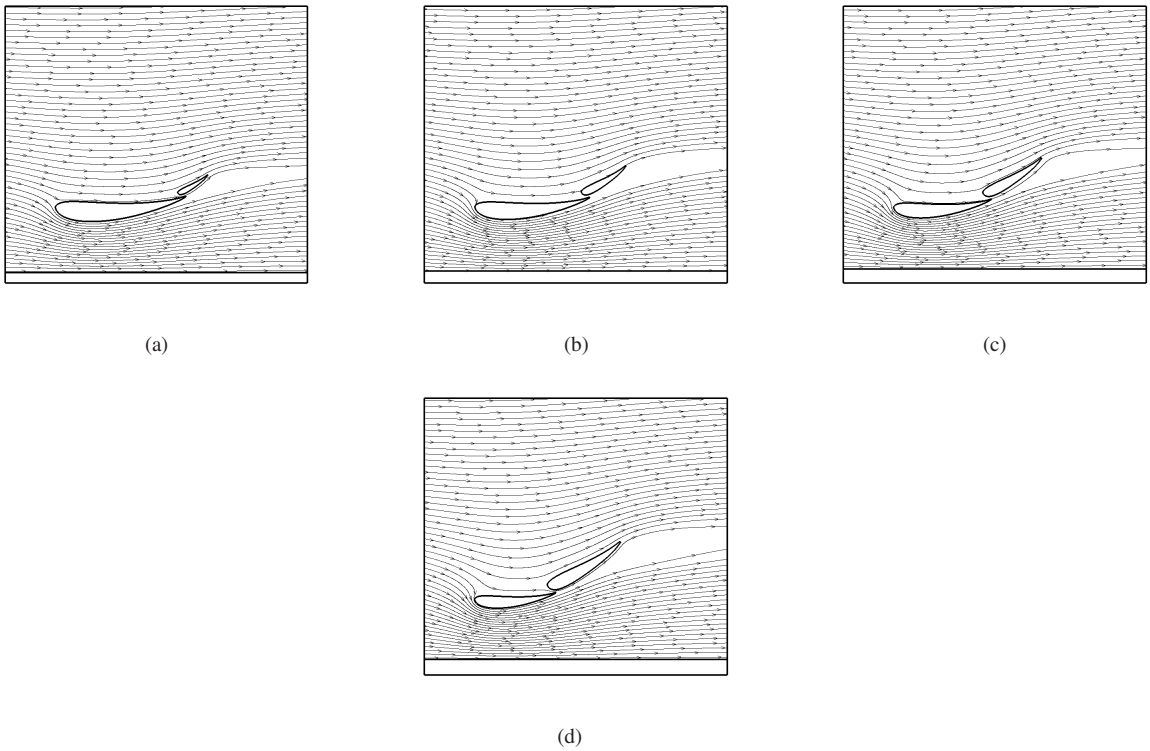

Figure 17. Diverging streamlines in the flap vicinity portraying wake deceleration with varying main element to system chord ratio: (a) 79% main element, (b) 69% main element, (c) 59% main element, and (d) 49% main element.

deflection angle will increase the suction peak on both the elements resulting in an increased C_l value and this can be seen by comparing the area enclosed within the C_p plots shown in Figs. 25a and 25b. Observing the pressure distribution plots in Figs. 25b and 25c around the flap, a general trend can be noticed that as the wake starts to thicken it suppresses the flap loads thus driving the pressure distribution to become comparatively flatter.

E. Effect of Gap

The UIUC1600 airfoil was simulated for different gap sizes varying from 0.07 in. to 0.84 in., while maintaining other baseline parameters as shown in Table 1. Figure 26 depicts velocity contours and represents the development of flowfield around the multielement airfoil geometry as the gap size is varied. The intensity of the warmer colors increases initially as the gap size is reduced to 0.63 in. and starts diminishing with further reduction in the same. For $l_{s,x}$ = 0.84 in., the blue region indicates highly-separated flow on the flap and small amount of wake bursting beneath the flap. As the gap size reduces to 0.63 in., a significant reduction in the separated region on the flap suction surface is observed, with separation point moving downstream near the trailing edge. Such delay in surface-flow separation occurs as a result of slat effect as described by Smith.[2] As the two airfoil elements move nearer to each other, the slat effect becomes stronger and reduces the flap suction peak, thus delaying separation. Also, with this reduction in gap size, the main element wake becomes thicker as depicted by the larger and more intense blue region beneath the flap indicating an increased amount of wake deceleration. The trend of increasing size and intensity of the blue region in the flap vicinity indicating stronger wake bursting continues as the gap size reduces further.

The trends discussed above can be explained with the aid of Fig. 27 which represents uniformly plotted streamlines around the multielement airfoil. For a large gap size the flap may experience a massive flow separation on its suction surface, as in the case of the $l_{s,x}$ = 0.84 in., thus reducing the curvature of the turn that the low momentum wake of the main element has to make around the flap. The resulting lower adverse pressure gradient that the main element wake experiences causes a reduction in the wake thickness. As the gap size is reduced to $l_{s,x}$ = 0.63 in., the separation on the flap suction side is delayed and hence the main element has to traverse a turn with a higher curvature, thus increasing

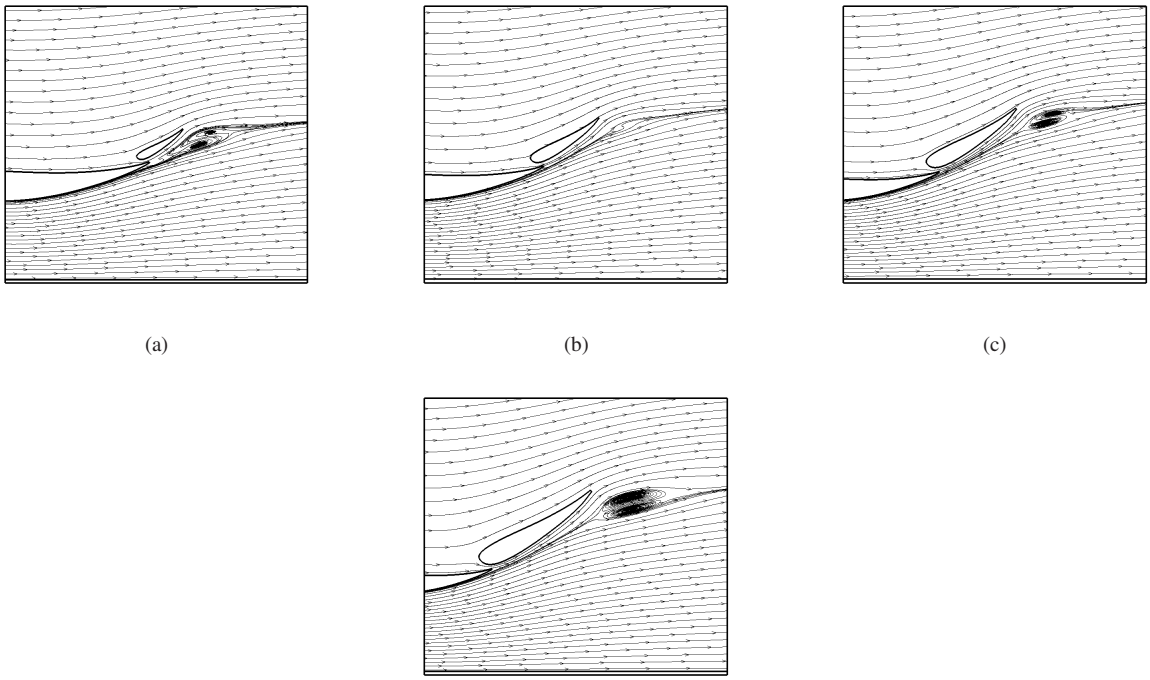

(a) (b) (c)

(d)

Figure 18. Flow reversal in the main element wake with varying main element to system chord ratio: (a) 79% main element, (b) 69% main element, (c) 59% main element, and (d) 49% main element.

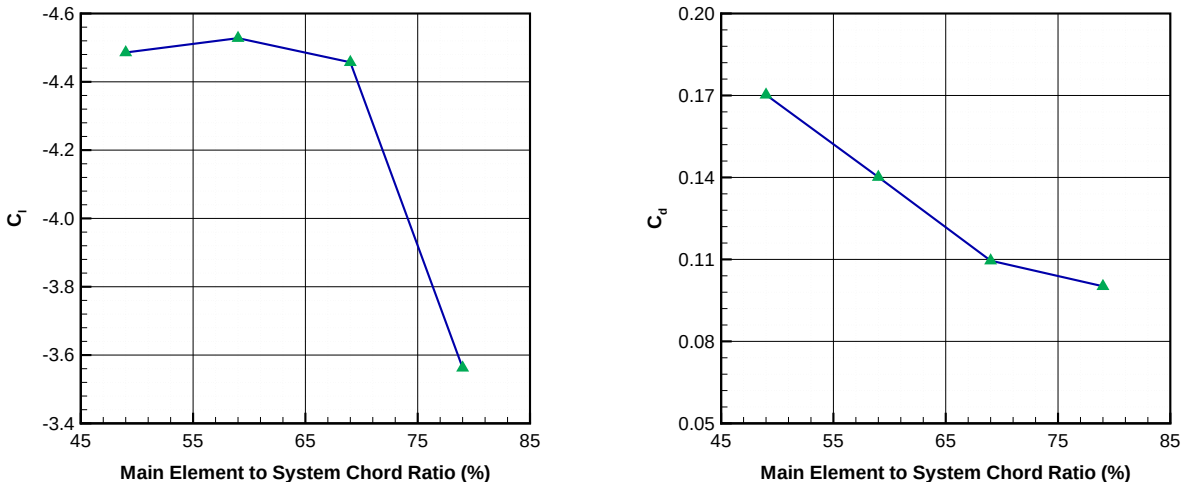

(a) (b)

Figure 19. Variation of C_l and C_d with main element to system chord ratio.

the adverse pressure gradient causing the wake to thicken. The trend continues until a gap size of 0.21 in. is achieved. Beyond this point, flow separation on the flap surface is zero and does not cause any major difference in the curvature of the main element wake path. But as it can be observed from Figs. 26 and 27, the wake still continues to grow in size with decreasing gap size thus indicating increasing amount of the wake bursting. The increased wake thickness

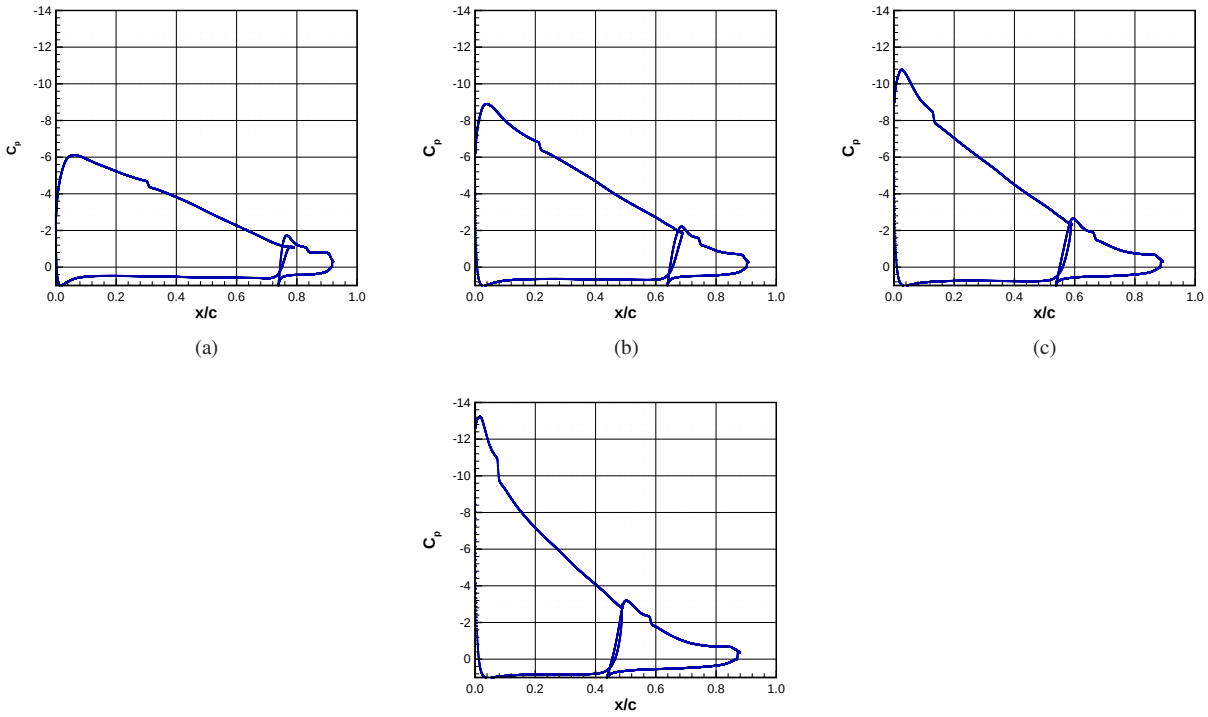

(a) (b) (c)

(d)

Figure 20. Variation in pressure distribution plots with different main element to system chord ratios: (a) 79% main element, (b) 69% main element, (c) 59% main element, and (d) 49% main element.

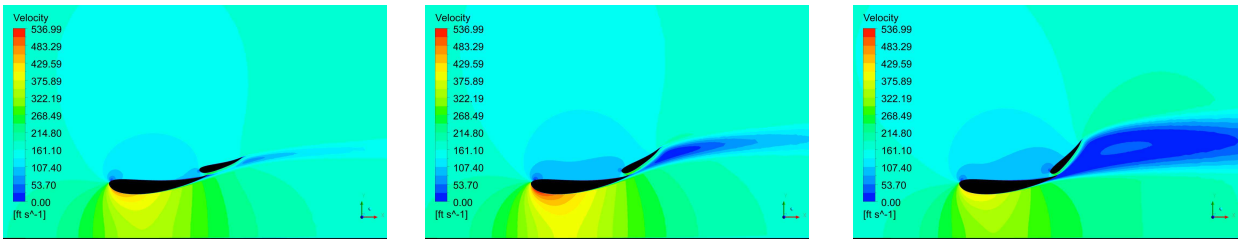

(a) (b) (c)

Figure 21. Velocity contours depicting effect of flap deflection angle on wake bursting: (a) $\delta_f = 12$ deg, (b) $\delta_f = 27$ deg, and (c) $\delta_f = 42$ deg.

occurs as a result of the obstruction to the slot flow due to low gap sizes.

In general, the flow around a flap for two element airfoils can be broken down into three distinct regions, 1) flap boundary layer, 2) flow through the slot, and lastly, 3) main element wake. A significant increase in the size of the burst wake can be explained with the aid of an interaction between these three flow regions. At larger gap sizes, large amounts of flow can be accelerated to a higher velocity resulting in a higher momentum of the slot flow. The high-momentum flow from the slot can exchange some of the momentum with the low-momentum main element wake, thus aiding the latter in better traversing the high adverse pressure gradient around the flap. Hence the velocity deficit gathered by the wake remains low, resulting in a thinner wake. This trend continues as the gap size is decreased until a critical gap size is reached. As the gap is reduced beyond the critical gap size, a large reduction in the mass flow rate causes a decrease in the slot flow momentum. The low-momentum flow from the slot becomes relatively inefficient in imparting some of its momentum to the main element wake, causing the latter to gather higher velocity deficit. The trend continues as the gap size is reduced further, and at a certain gap size the momentum exchange between the flow through the slot and the burst wakes can be significantly low causing off-the-surface flow reversal in the latter. For

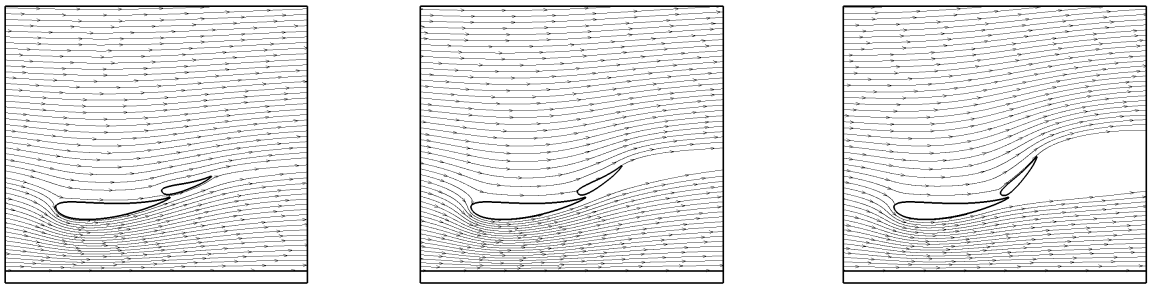

(a) (b) (c)

Figure 22. Diverging streamlines in the vicinity of the flap due to wake deceleration shown for three flap deflection angles: (a) δ_f = 12 **deg, (b)** δ_f = 27 **deg, and (c)** δ_f = 42 **deg.**

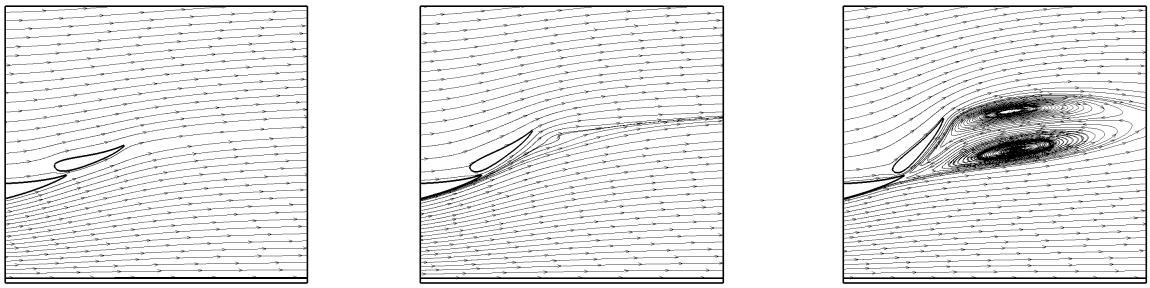

(a) (b) (c)

Figure 23. Flow structure within the burst wakes shown for three flap deflection angles: (a) δ_f = 12 **deg, (b)** δ_f = 27 **deg, and (c)** δ_f = 42 **deg.**

very small gap sizes such as 0.07 in., the burst wakes become large enough to cause confluence with the flap boundary layer. The confluence causes the flap pressure distribution to become much flatter, thus accounting for the low value of C_l as seen from Fig. 29.

Observing the streamlines passing through the gap in Fig. 27, the reason for flap pressure peak reduction with decreasing gap size can be deduced. For large gap sizes such as $l_{s,x}$ = 0.84 in., and $l_{s,x}$ = 0.63 in., the streamlines passing through the slot have to turn around the suction surface of the flap having higher curvature causing a high suction peak. At lower gap sizes, one can notice that a larger portion of the flow, earlier passing through the slot, is diverted toward the pressure side of the flap having lower curvature causing a pressure peak reduction as seen in Fig. 30. Also, as discussed earlier, a gap size smaller than 0.63 in. results in lower momentum in the flow through the slot and causes wake bursting to increase. The combined effect of the reduced curvature in the flow and a lower mass flow rate through the slot causes a flatter pressure distribution on the flap suction side, as seen from Figs. 30c–30e.

The importance of the gap size on wake bursting can be seen from Fig. 28 which depicts the streamlines around the flap in greater detail. For the 0.84 in. gap size, a massive flow separation as discussed previously can be seen in Fig. 28a. With this gap size reduced further, the separation on the flap suction side is delayed and the streamlines in the flap vicinity can be seen diverging as a result of increased wake deceleration. When the gap size is reduced to 0.14 in., the flow in the main element wake separates from itself resulting in formation of two distinct vortices having nearly equal size. On reducing the gap size to 0.07 in., the upper vortex breaks into two smaller ones while the lower vortex merges with the separated flow on the main element suction side. The burst main element wake becomes confluent with the flap boundary layer at such a small gap size and causes a significant flap load reduction as seen in Fig. 30e.

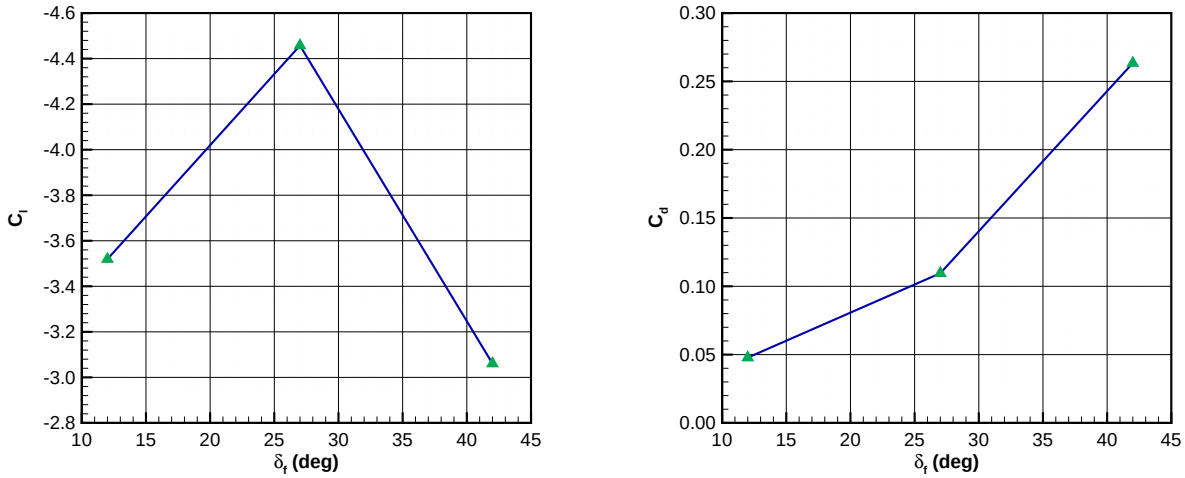

(a) (b)

Figure 24. Variation of C_l and C_d with flap deflection angle.

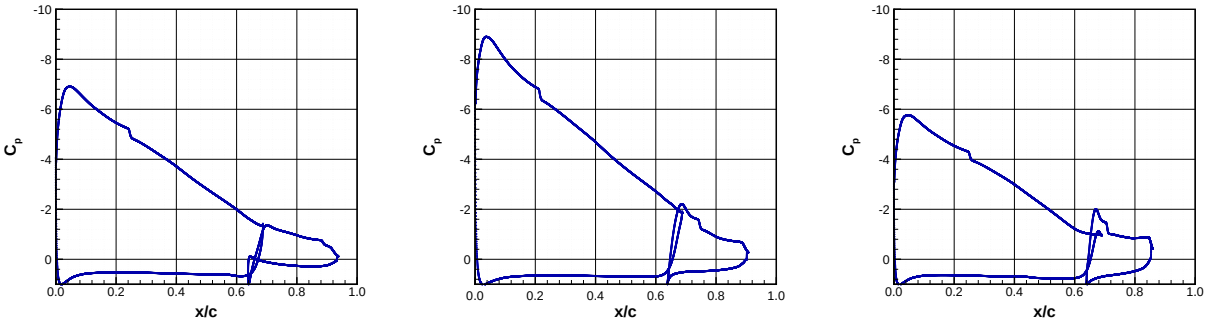

(a) (b) (c)

Figure 25. Variation of C_p distribution with flap deflection angle: (a) $\delta_f = 12$ deg, (b) $\delta_f = 27$ deg, and (c) $\delta_f = 42$ deg.

IV. Conclusions

A computational study of the wake bursting was performed for varying inverted multielement configurations in ground effect to identify the wake-bursting amplifying configurations, and to study the effect of off-the-surface flowfield on the performance of these configurations. The following conclusions are made:

- Decreasing the ground clearance height of the airfoil system led to an initial increment in the downforce coefficient C_l produced until a critical height was reached, beyond which downforce reduction was observed. The reduction in the C_l value with further decreasing ground clearance height is attributed to a combination of large areas of separated flows on both the main element suction side and increased amount of the main element wake bursting as a result of increasing adverse pressure gradient on the airfoil suction surfaces.

- Increasing the main element angle of attack, while maintaining the same ground clearance and other parameters led to an increase in the amount of downforce generated until a critical angle was reached beyond which loss of downforce was observed. This reduction in downforce, however, did not precipitate as a result of surface flow separation, but because of increased wake bursting. Interestingly, no flow reversal was observed in the main element wake indicating that wake bursting, even without any flow separation either on the airfoil surface or within the wake, can be significant enough to cause the downforce reduction of an inverted multielement airfoil

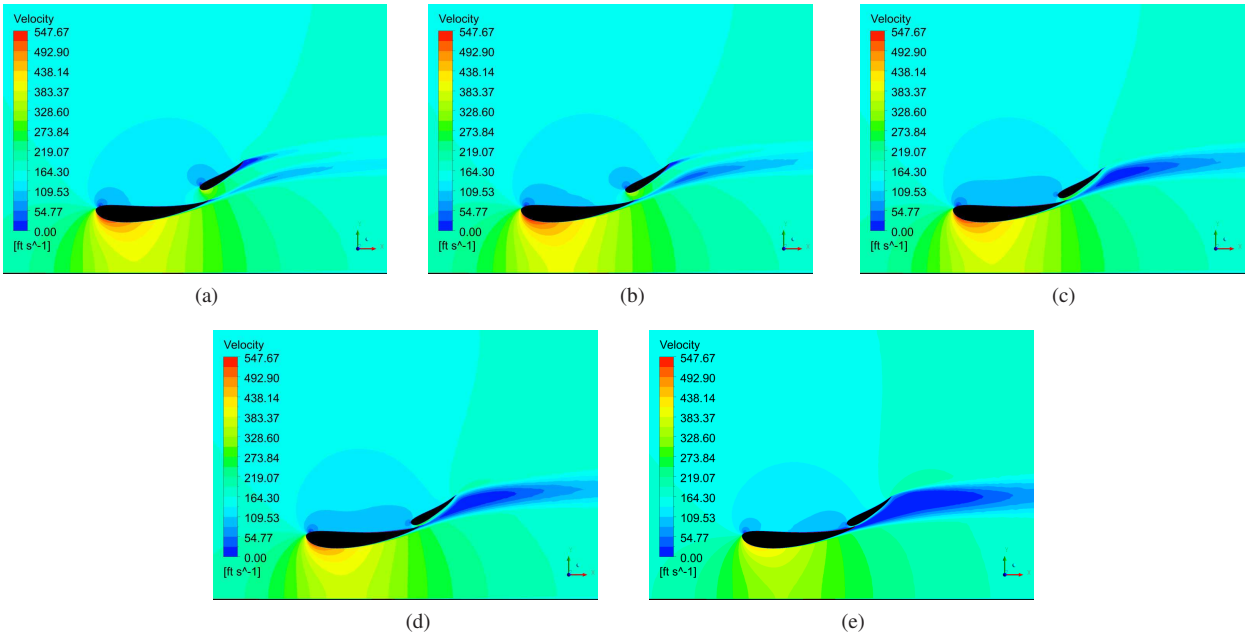

Figure 26. Velocity contours depicting effect of varying gap size on wake bursting for seven different gap sizes: (a) $l_{s,y} = 0.84$ **in., (b)** $l_{s,y} = 0.63$ **in., (c)** $l_{s,y} = 0.21$ **in., (d)** $l_{s,y} = 0.14$ **in., and (e)** $l_{s,y} = 0.07$ **in.**

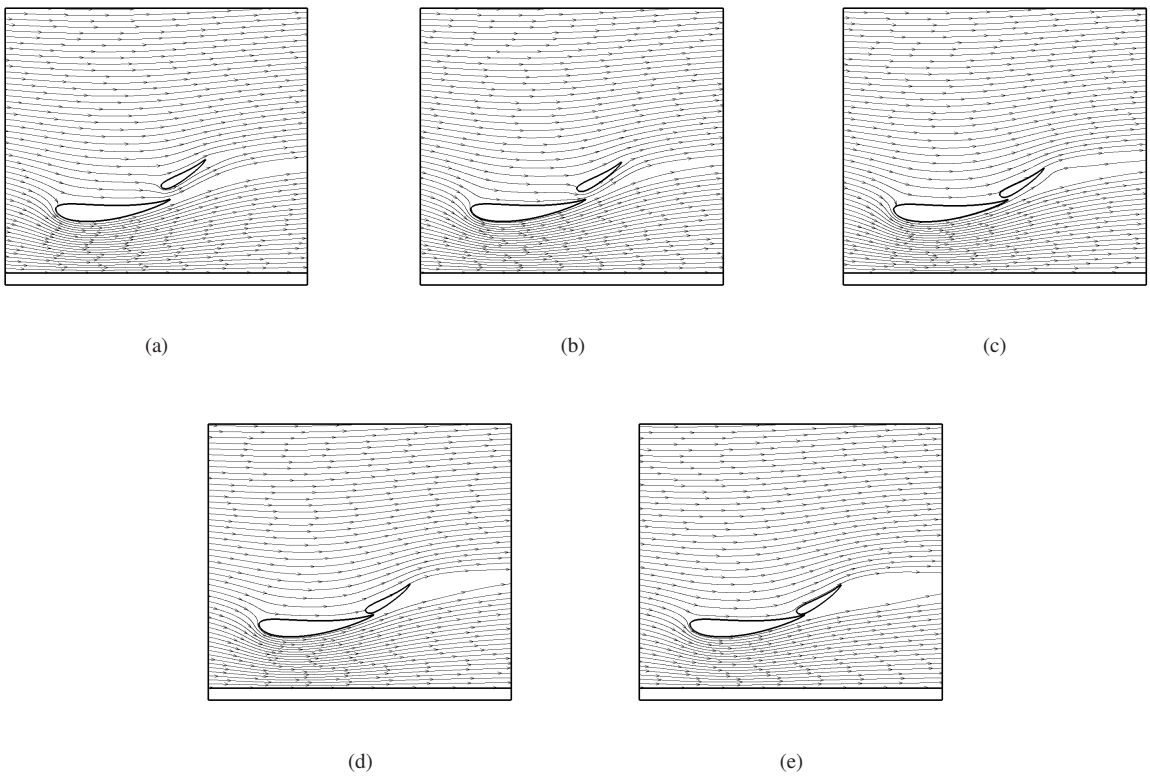

Figure 27. Streamlines for the dual element airfoil for five gap sizes: (a) $l_{s,y} = 0.84$ **in., (b)** $l_{s,y} = 0.63$ **in., (c)** $l_{s,y} = 0.21$ **in., (d)** $l_{s,y} = 0.14$ **in., and (e)** $l_{s,y} = 0.07$ **in.**

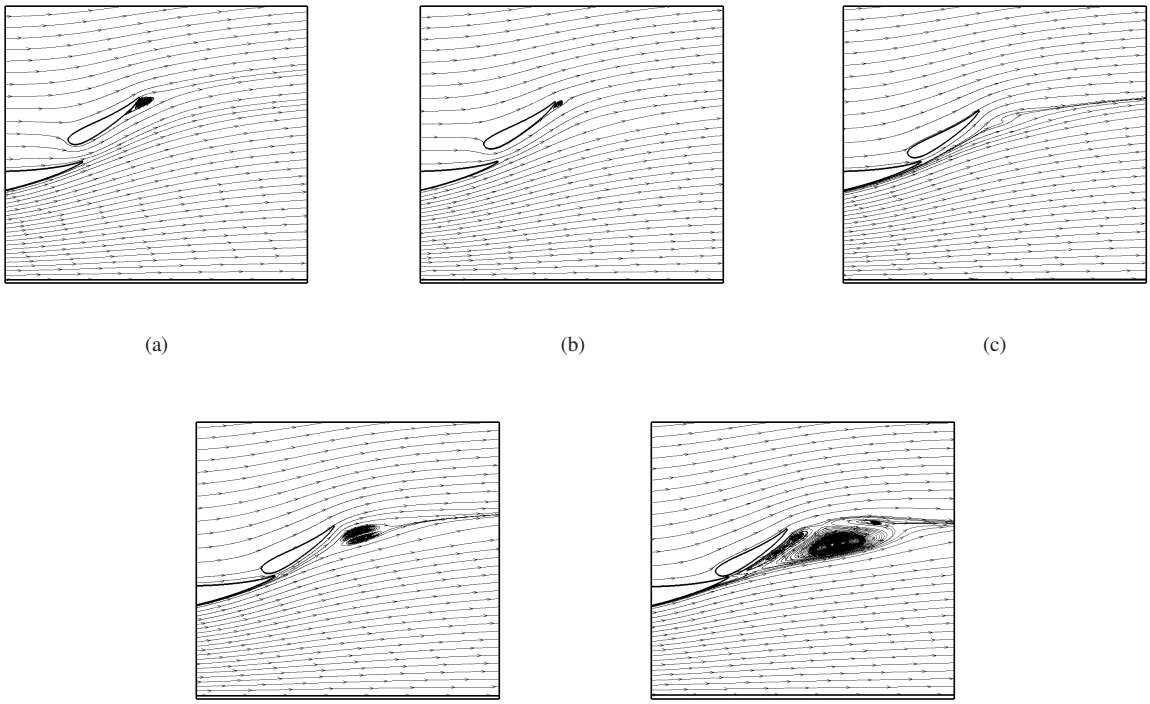

(a) (b) (c)

(d) (e)

Figure 28. Effect of gap size on the degree of wake bursting, as shown by streamlines in the flap vicinity: (a) $l_{s,y} = 0.84$ **in., (b)** $l_{s,y} = 0.63$ **in., (c)** $l_{s,y} = 0.21$ **in., (d)** $l_{s,y} = 0.14$ **in., and (e)** $l_{s,y} = 0.07$ **in.**

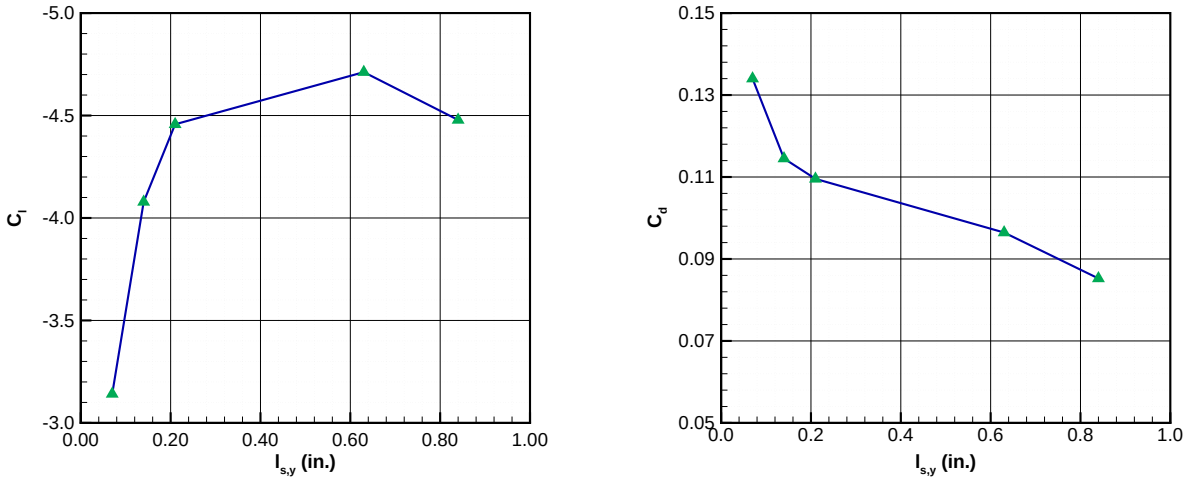

(a) (b)

Figure 29. Plots of C_l **and** C_d **versus gap size** $l_{s,y}$**: (a)** C_l **vs** $l_{s,y}$ **and (b)** C_d **vs** $l_{s,y}$**.**

operating in ground effect. Increasing the flap deflection angle increased C_l while also increasing the wake thickness.

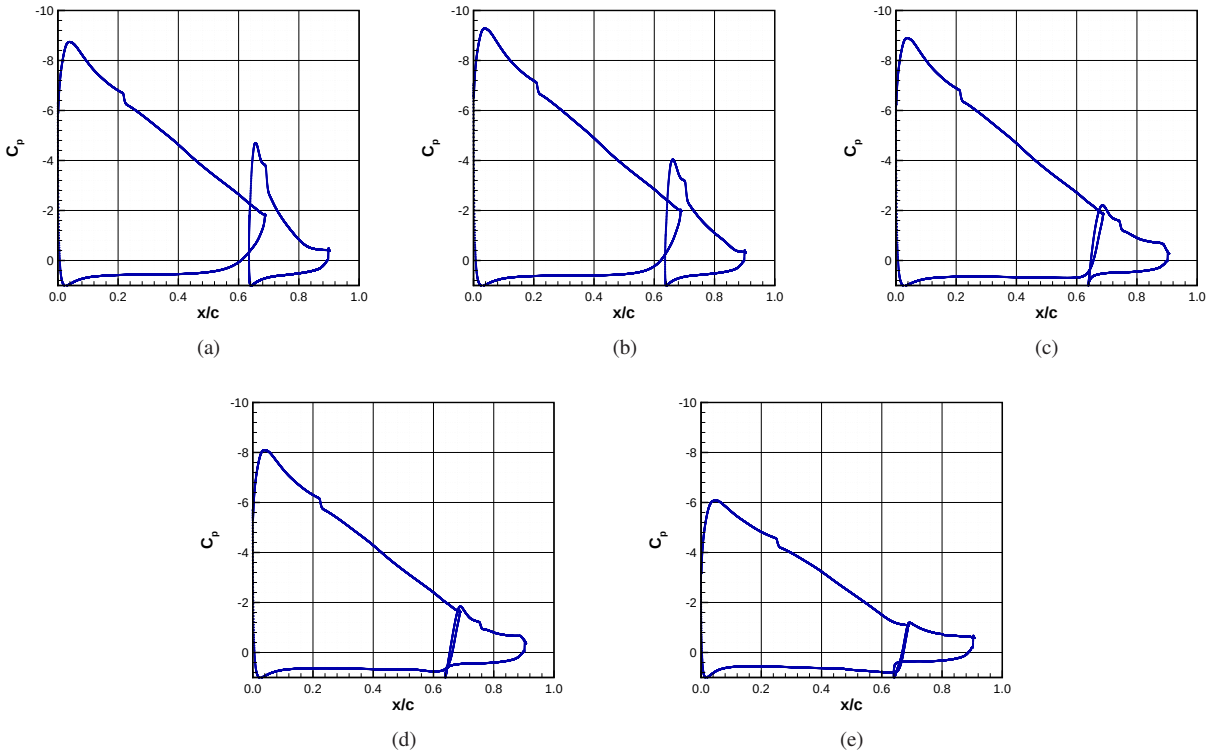

Figure 30. A plot of pressure distribution C_p vs x/c for five different gap sizes: (a) $l_{s,y} = 0.84$ in., (b) $l_{s,y} = 0.63$ in., (c) $l_{s,y} = 0.21$ in., (d) $l_{s,y} = 0.14$ in., and (e) $l_{s,y} = 0.07$ in.

- Decreasing the main element to system chord ratio, thus making the flap larger in size, had the effect of increasing the suction peak heights on both the main element and the flap. However, an increment in the suction peak over the airfoil surfaces was countered by a flatter pressure distribution on the flap surface due to increased wake bursting, causing the rate at which the C_l increases with increasing flap size, to fall. For the larger flap sizes, wake bursting was found to be significant enough to cause the C_l to be almost same as the one for a slightly smaller flap size, while increasing the C_d significantly.

- Decreasing the gap size had the effect of increasing the downforce initially, until an optimum gap size was achieved. Reducing the gap size further had the effect of reducing the amount of flow mass through the slot causing some of the flow, earlier passing through the slot, to flow over the lower-curvature pressure-side of the flap instead of the higher-curvature suction side. The reduced mass flow rate coupled with a lowered slot flow acceleration caused the wake bursting to increase and hence affected the flap pressure distribution further. The resulting suppression of the flap loading with further reduction in the gap size caused a dramatic decrease in C_l. At a certain small gap size, flow reversal in the wake was observed.

- In general, it can be concluded that off-the-surface flowfield has a significant effect on the surface pressure distribution and performance of an inverted multielement airfoil in ground effect. The effect of increased wake bursting was to flatten the pressure distribution on the flap causing the C_l to be lower. The pressure distribution near the trailing edge of the airfoil was also flattened significantly when the burst wake merged with the separated flow on the main element suction surface near its trailing edge.

- Wake bursting, as seen in the case of low ground clearances and extremely small gap sizes, can create a large areas of recirculation region within the wake which may interfere with the aerodynamic performance of the racecar components operating in the wake of the front wing. Also, it is hypothesized that this large sensitivity of the size of the burst wake with ground clearance can alter the flowfield of these downstream racecar components whenever a racecar experiences even a slight amount of pitching due to braking or other reasons. Keeping these

reasons in mind, it becomes apparent that tuning the front wing wake structure is very important for an optimum overall aerodynamic performance of a racecar.

V. Acknowledgment

The authors would like to extend appreciation to Brent Pomeroy, graduate student at the University of Illinois at Urbana-Champaign for numerous insightful and valuable discussions regarding computational grids and turbulence models required to simulate and accurately capture all the immensely intricate aspects of high-lift flows.

References

[1]Agathangelou, B. and Gascoyne M. Aerodynamic Considerations of a Formula 1 Racing Car. SAE Technical Paper 980399, 1998.

[2]Smith, A.M.O. High Lift Aerodynamics. *Journal of Aircraft*, Vol. 12(6):501–530, June 1975.

[3]van Dam, C. P. The Aerodynamic Design of Multi-Element High-Lift Systems for Transport Airplanes. *Progress in Aerospace Sciences*, Vol. 38:101–144, 2002.

[4]Ranzenbach, R. and Barlow, J. B. Multi-Element Airfoil in Ground Effect – An Experimental and Computational Study. AIAA Paper 97-2238, 1997.

[5]Soso, M. and Wilson, P. Investigating Changes to the Downforce Curve of a Double Element Airfoil in Ground Effect. SAE Technical Paper 2004-01-3558, 2004.

[6]Nakayama, A., Kreplin, H. P., and Morgan, H. L. Experimental Investigation of Flowfield about a Multielement Airfoil. *AIAA Journal*, Vol. 28(1):14–21, 1988.

[7]Hoffenberg, R. and Sullivan, J. P. Measurement and Simulation of Wake Deceleration. AIAA Paper 98-0522, 1998.

[8]Klausmeyer, S. M. and Lin, J. C. An Experimental Investigation of Skin Friction on a Multi-Element Airfoil. AIAA Paper 94-1870, 1994.

[9]Hoffenberg, R. and Sullivan, J. P. Simulation of High-Lift Wake Behavior. AIAA Paper 97-0718, 1997.

[10]Spaid, F. W. High Reynolds Number, Multielement Airfoil Flowfield Measurements. *Journal of Aircraft*, Vol. 37(3):499–507, 2000.

[11]Rogers, S. E. Progress in High-Lift Aerodynamic Calculations. *Journal of Aircraft*, Vol. 31(6):1244–1251, 1994.

[12]Cebeci, T., Besnard, E., and Chen, H. H. Calculation of Multielement Airfoil Flows, Including Flap Wells. AIAA Paper 96-0056, 1996.

[13]Czerwiec, R. and Edwards, J. R. Theory and Experiment of Multielement Airfoils – A Comparison. AIAA Paper 2000-0985, 2000.

[14]Narsipur, S., Pomeroy, B. W., and Selig, M. S. CFD Analysis of Multielement Airfoils for Wind Turbines. AIAA Paper 2012-2781, 2012.

[15]Chin, V. D. Flowfield Measurements about a Multi-Element-Element Airfoil at High Reynolds Number. AIAA Paper 93-3137, 1993.

[16]Pomeroy, B. W. and Selig, M. S. Pressure Measurement of Burst Wakes over a Three-Element Airfoil. AIAA Paper 2015-2596, 2015.

[17]Johnston, L. J. and Horton, H. P. An Experimental Study of Turbulent Wake/Boundary-Layer Mixing Flows. *Proceedings of the International Council of the Aeronautical Sciences*, pages 360–369, 1986.

[18]Mahon, S. and Zhang, X. Computational Analysis of a Inverted Double-Element Airfoil in Ground Effect. *Journal of Fluids Engineering*, Vol. 128(6):1172–1180, 2006.

[19]Carroll, C. High Downforce Airfoils in Ground Effect: A Trade Study for Use in Open-Wheeled Racecar Front-Wing Design. Master's thesis, Department of Aerospace Engineering, University of Illinois at Urbana-Champaign, Urbana, IL 61801, USA, 2005.

[20]Rumsey, C. L. and Slotnick, J. P. Overview and Summary of the Second AIAA High-Lift Prediction Workshop. *Journal of Aircraft*, Vol. 52 (No. 4):1006–1025, 2015.

[21]Menter, F. R., Smirnov, P. E., Liu, T., and Avancha R. A One-Equation Local Correlation-Based Transition Model. *Flow, Turbulence and Combustion*, Vol. 95(4):583–619, 2015.

[22]Celik, I., Ghia, U., Roache, P., and Freitas, C. Procedure for Estimation and Reporting of Uncertainty Due to Discretization in CFD Applications. *Journal of Fluids Engineering*, 10(7):1–4, July 2008.

[23]Roache, P. J. Perspective: A Method for Uniform Reporting of Grid Refinement Studies. *Journal of Fluids Engineering*, 116:405–413, Sept. 1994.

Appendix A:
UIUC1600 Airfoil Coordinates

Main Element	
x/c	y/c
1.003034	0.006246
0.999319	0.007531
0.989572	0.012030
0.975557	0.018469
0.957953	0.025924
0.936320	0.034018
0.910278	0.042908
0.880138	0.052647
0.846139	0.062612
0.808722	0.072642
0.768345	0.082551
0.725503	0.092152
0.680709	0.101238
0.634492	0.109601
0.587398	0.117003
0.539860	0.123129
0.492216	0.127839
0.444884	0.131120
0.398328	0.132927
0.352977	0.133211
0.309218	0.131967
0.267412	0.129184
0.227859	0.124896
0.190829	0.119114
0.156511	0.111869
0.125112	0.103244
0.096844	0.093238
0.071904	0.081863
0.050462	0.069145
0.032660	0.055257
0.018622	0.040471
0.008450	0.025478
0.002223	0.010837
0.000000	-0.002593
0.003391	-0.013255
0.013168	-0.002593
0.028253	-0.030070
0.048202	-0.035317
0.072745	-0.038100
0.101742	-0.038362
0.135139	-0.036383
0.172864	-0.032463
0.214888	-0.027029
0.260995	-0.020651
0.310781	-0.013704
0.363769	-0.006527
0.419390	0.000617
0.477123	0.007501
0.536378	0.013636
0.596136	0.018377
0.655152	0.021545
0.715303	0.023142
0.766561	0.023270
0.816996	0.022079
0.862770	0.019761
0.903114	0.016529
0.937334	0.012642
0.964713	0.008325
0.984378	0.004154
0.999999	0.000186
1.003034	0.006246

Flap Element

x/c	y/c
1.005497	0.014626
0.996399	0.018084
0.981391	0.023765
0.964781	0.030018
0.947017	0.036665
0.928978	0.043309
0.910907	0.049372
0.892022	0.054900
0.872104	0.060186
0.851448	0.065190
0.830038	0.069914
0.807834	0.074403
0.784972	0.078651
0.761554	0.082648
0.737610	0.086404
0.713202	0.089929
0.688404	0.093223
0.663260	0.096293
0.637782	0.099150
0.611953	0.101816
0.585811	0.104324
0.559491	0.108900
0.533182	0.110931
0.507070	0.110931
0.481223	0.112739
0.455596	0.114306
0.430188	0.115631
0.405068	0.116703
0.380280	0.117505
0.355846	0.118301
0.331829	0.118277
0.308335	0.118236
0.285450	0.117902
0.263253	0.117273
0.241884	0.116362
0.221507	0.115172
0.202213	0.113697
0.184034	0.111946
0.167029	0.109948
0.151255	0.107725
0.136706	0.105283
0.123321	0.102633
0.111033	0.099796
0.099775	0.096797
0.089481	0.093656
0.080080	0.090387
0.071496	0.087005
0.063661	0.083523
0.056510	0.079953
0.049984	0.076308
0.044033	0.072597
0.038609	0.068825
0.033668	0.064999
0.029174	0.061125
0.025098	0.057210
0.021409	0.053261
0.018081	0.049283
0.015093	0.045283
0.012422	0.041279
0.010048	0.037262
0.007961	0.033214
0.006154	0.029224
0.004621	0.025219
0.003351	0.021234
0.002325	0.017286
0.001517	0.013385
0.000906	0.009532
0.000478	0.005716
0.000241	0.001923
0.000227	-0.001854
0.000468	-0.005627
0.001000	-0.009412
0.001860	-0.013175
0.003083	-0.016834
0.004715	-0.020303
0.006804	-0.023498
0.009332	-0.026412
0.012248	-0.029066
0.015482	-0.031492
0.018983	-0.033718
0.022767	-0.035754
0.026856	-0.037618
0.031278	-0.039330
0.036066	-0.040909
0.041267	-0.042364
0.046929	-0.043705
0.053101	-0.044952
0.059838	-0.046106
0.067209	-0.047149
0.075299	-0.048059
0.084215	-0.048810
0.094092	-0.049383
0.105071	-0.049762
0.117283	-0.049931
0.130839	-0.049856
0.145830	-0.049859
0.162334	-0.048838
0.180370	-0.047844
0.199866	-0.046508
0.220686	-0.044817
0.242176	-0.042768
0.265851	-0.040376
0.289937	-0.037675
0.314821	-0.034694
0.340411	-0.031463
0.366614	-0.028026
0.393263	-0.024459
0.420160	-0.020880
0.447128	-0.017397
0.474038	-0.014054
0.500830	-0.010874
0.527487	-0.007871
0.553996	-0.005059
0.580348	-0.002449
0.606547	-0.000054
0.632594	0.002120
0.658473	0.004066
0.684144	0.005772
0.709564	0.007226
0.734688	0.008418
0.759436	0.009340
0.783672	0.009985
0.807228	0.010346
0.829917	0.010424
0.851500	0.010222
0.871693	0.009759
0.890316	0.009064
0.907367	0.008172
0.922844	0.007191
0.936625	0.006253
0.948716	0.005396
0.959326	0.004573
0.968707	0.003780
0.977013	0.003110
0.984367	0.002618
0.991003	0.001938
0.997219	0.000517
1.002274	0.000424
1.005258	0.005167
1.005497	0.014626